AD-A185 005   THEORY OF INDUCED SPATIAL INCOHERENCE(U) NAVAL RESEARCH   1/1
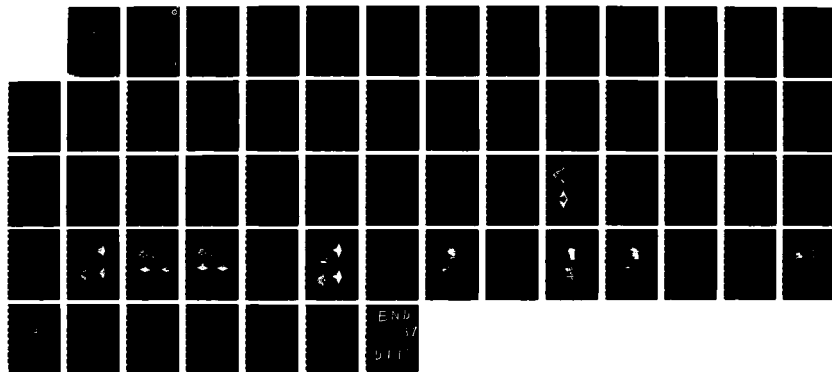LAB WASHINGTON DC   R H LEHMBERG ET AL   16 SEP 87
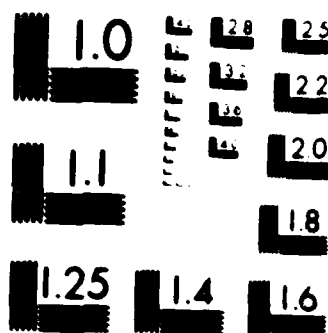NRL-MR-5980

UNCLASSIFIED   F/G 18/1   NL

END
87
DTIC

Naval Research Laboratory

Washington, DC 20375-5000

BTIC FILE COPY

AD-A185 005

Theory of Induced Spatial Incoherence

R. H. LEHMBERG, A. J. SCHMITT AND S. E. BODNER

Laser Plasma Branch
Plasma Physics Division

September 16, 1987

DTIC
ELECTE
SEP 2 5 1987
E

87 9 18 007

ADA185005

REPORT DOCUMENTATION PAGE

1a. REPORT SECURITY CLASSIFICATION UNCLASSIFIED	1b. RESTRICTIVE MARKINGS
2a. SECURITY CLASSIFICATION AUTHORITY	3 DISTRIBUTION / AVAILABILITY OF REPORT Approved for public release; distribution unlimited.
2b. DECLASSIFICATION / DOWNGRADING SCHEDULE	

4. PERFORMING ORGANIZATION REPORT NUMBER(S) NRL Memorandum Report 5980	5. MONITORING ORGANIZATION REPORT NUMBER(S)

6a. NAME OF PERFORMING ORGANIZATION Naval Research Laboratory	6b. OFFICE SYMBOL (If applicable)	7a. NAME OF MONITORING ORGANIZATION

6c. ADDRESS (City, State, and ZIP Code) Washington, DC20375-5000	7b. ADDRESS (City, State, and ZIP Code)

8a. NAME OF FUNDING / SPONSORING ORGANIZATION Department of Energy	8b. OFFICE SYMBOL (If applicable)	9. PROCUREMENT INSTRUMENT IDENTIFICATION NUMBER

8c. ADDRESS (City, State, and ZIP Code) Washington, DC	10. SOURCE OF FUNDING NUMBERS			
	PROGRAM ELEMENT NO.	PROJECT NO.	TASK NO.	WORK UNIT ACCESSION NO.

11. TITLE (Include Security Classification)

Theory of Induced Spatial Incoherence

12. PERSONAL AUTHOR(S)
Lehmberg, R.H., Schmitt, A.J., and Bodner, S.E.

13a. TYPE OF REPORT Interim	13b. TIME COVERED FROM _____ TO _____	14. DATE OF REPORT (Year, Month, Day) 1987 September 16	15. PAGE COUNT 61

16. SUPPLEMENTARY NOTATION

17. COSATI CODES			18. SUBJECT TERMS (Continue on reverse if necessary and identify by block number)
FIELD	GROUP	SUB-GROUP	Laser Fusion
			Uniform Illumination
			Spatial incoherence

19. ABSTRACT (Continue on reverse if necessary and identify by block number)

This paper describes theoretical and experimental investigations of induced spatial incoherence (ISI), a technique for achieving the smooth and controllable target beam profiles required for direct-drive laser fusion. In conventional ISI, a broadband laser beam (coherence time $t_c = 1/\Delta\nu << t_{pulse}$) is sliced into an array of mutually-incoherent beamlets by echelon structures that impose successive time delay increments $\Delta t > t_c$. A focusing lens then overlaps those beamlets onto the target, which is usually located at the far field. Here, we evaluate the ideal target beam profiles for practical ISI focusing configurations, and examine the perturbing effects of transient interference, laser aberration, and plasma filamentation. Analytic and numerical calculations show that nonuniformities due to interference among the beamlets are smoothed by both thermal diffusion and temporal averaging. Under laser-plasma conditions of interest to ICF, average ablation pressure nonuniformities ~ 1% should be readily attainable. We also investigate a partial ISI scheme, which allows

(Continued)

20. DISTRIBUTION / AVAILABILITY OF ABSTRACT ☒ UNCLASSIFIED/UNLIMITED ☐ SAME AS RPT. ☐ DTIC USERS	21. ABSTRACT SECURITY CLASSIFICATION UNCLASSIFIED
22a. NAME OF RESPONSIBLE INDIVIDUAL R.H. Lehmberg	22b. TELEPHONE (Include Area Code) (202) 767-2730 22c. OFFICE SYMBOL Code 4730

DD FORM 1473, 84 MAR   83 APR edition may be used until exhausted.
All other editions are obsolete.

19. ABSTRACTS (Continued)

widely-spaced beamlets to remain mutually-coherent; the resulting high spatial frequency interference struc-
ture can be effectively smoothed by thermal diffusion alone. A perturbation analysis shows that the average
target profile $\langle I(x) \rangle$ remains relatively insensitive to laser beam aberration when the scalelength of that aberra-
tion is larger than the initial beamlet width. This aberration will tend to broaden and smooth $\langle I(x) \rangle$, rather
than introduce any small-scale structure. The broadening is largely controllable because it depends only upon
spatial averages of the aberrated quantities over the entire laser aperture; the uncontrollable perturbations can
be reduced to $\sim 1\%$ in practical cases. Filamentation in the underdense plasma has been studied numerically
using a 2D propagation/hydro code SELFOCT, which includes both ponderomotive and thermal effects. For
0.25 μm light, this code predicts that ISI should suppress filamentation in plasmas of interest to ICF. We
review recent NRL planar target experiments at 1.054 and 0.527 μm, which show that the combination of ISI
and shorter wavelength substantially reduces all evidence of plasma instabilities. Finally, we review a
promising alternative technique for achieving ISI in KrF lasers without using echelons.

CONTENTS

THEORY OF INDUCED SPATIAL INCOHERENCE

I. INTRODUCTION

High gain laser fusion requires a highly symmetric pellet implosion, with ablation pressure nonuniformities of no more than a few percent around the spherical surface.[1,2] For directly-driven pellets, this symmetry must be achieved by the combination of nearly uniform laser illumination and thermal diffusion in the ablating plasma.[3] Thermal diffusion alone is ineffective in reducing lower spatial frequency nonuniformities to acceptable levels, especially at the short optical wavelengths required for good laser-target coupling.[4,5]

Theoretical studies have shown that acceptable spherical illumination uniformity can be achieved by overlapping a limited number (≥ 20) of focused beams, provided that each individual beam profile is smooth and controllable.[6-9] Earlier efforts to obtain such profiles, however, have been frustrated by the inherent imperfections in high-power multistage laser systems. The cumulative effect of numerous small amplitude and phase aberrations (both linear and nonlinear) introduced by each optical element of a multistage laser produces large random aberrations in the output beam, and hence large random intensity nonuniformities at the target surface. Efforts to control laser aberrations, using ultra high quality optics and extensive beam relaying, have not been completely successful, especially at high energies and shorter laser wavelengths.[10,11] Nonlinear optical techniques, such as phase conjugation[12] and Raman beam cleanup,[13-15] are effective at generating beams capable of producing nearly diffraction—limited focal spots. However, these techniques are not generally effective in eliminating large residual intensity nonuniformities in the quasi near-field of the laser,[14-16] where the pellet would have to be placed in order to obtain the required spot size with a lens of reasonable focal length.

One promising solution to the uniformity problem is the Induced Spatial Incoherence (ISI) concept.[17-21] In the conventional version[17-20] of this technique, a broadband laser beam (bandwidth $\Delta \nu >> 1/t_{pulse}$) is sliced into an array of small beamlets by an orthogonal pair of echelon structures, which impose a different time delay at each step. (The idea is illustrated in two dimensions in Fig. 1.) If the delay increments $\Delta t = t_{n+1} - t_n$ are chosen somewhat longer than the optical coherence time $t_c = 1/\Delta \nu$, the beamlets become mutually incoherent. These beamlets are then overlapped onto the target by a lens of focal length f. Each of them will independently focus to the same smoothly-varying far-field diffraction profile of total width $2f\lambda/D_1$, provided that the initial width D_1 is small in comparison to the aberration scalelength s_{ab} in the incident laser beam. One has the option of either centering all of the profiles at a single point, or (by slightly tilting adjacent echelon steps in opposite directions) centering them equally around four nearby quadrature points in order to control the shape and width of the composite profile.[18-20] (Fig. 2) If the incident beam aberration also contains some short scalelength components ($s'_{ab} << D_1$), which might for example arise from hard apertures or damage spots, the resulting energy will tend to focus well outside the main lobe of the far-field diffraction pattern. This component will therefore miss the target, and will be of little consequence as long as it represents only a small fraction of the total energy.

Although the overlapped beamlets produce a complicated interference pattern at any one instant. their mutual incoherence ensures that this pattern will evolve randomly in times of order t_c. If the target responds hydrodynamically. in times $\sim t_{hydro} >> t_c$. it will effectively ignore this rapidly-shifting structure. and respond only to the smooth time-averaged diffraction profile. For example. an optical bandwidth $\Delta \nu = 30$ cm^{-1} (easily achieved in Nd glass or KrF lasers) provides $t_c = 1$ ps. whereas time scales for gross hydrodynamic motion of a large high gain pellet shell are typically ~ 1 to 10 ns.

The idea of slicing the laser light into beamlets that are subsequently integrated at the target plane also forms the basis of several other techniques for controlling irradiation profiles. In the random-phase shift (RPS) technique developed by Kato and Mima.[22,23] the beam slicing is performed by a transparent phase mask.[24] which randomly imposes a fixed phase shift of either 0 or π on each of the resulting beamlets. The RPS technique has the advantage that it does not require a broadband laser. and the phase mask may. in some existing laser facilities. be easier to utilize than ISI echelons. However. the fixed phase relationship among the beamlets (even with broadband light) ensures that the interference pattern will remain stationary throughout the pulse duration. The lower spatial frequency components of this pattern could not only create nonuniformities in the ablation pressure. but could also seed self focusing or other instabilities in the underdense plasma.

Several optical integrating techniques have been developed to produce a "flat-topped" intensity profile at the target. This can be accomplished by an array of prisms.[25] tilted mirrors,[26,27] or lens systems[28] that combine the beamlets in their quasi-near fields. With these techniques one can avoid most of the deleterious low spatial frequencies in the interference pattern if one also uses low F/number optics (i.e., large angles between the beamlets). Alternatively, one can achieve full ISI operation by using a broadband laser and allowing the usual delay increments between the tilted echelon steps. as illustrated in Fig. 3. All of these quasi near-field schemes have the drawback that Fresnel diffraction of the sharp-edged beamlets will introduce gross nonuniformities unless the Fresnel numbers are > 100. This requires very low F/number optics, which would be unsuitable for a reactor design.[8] In principle, both Fresnel ripples and short scalelength intensity aberrations can be at least partially averaged out by offsetting the beamlets from one another at the target.[28] However. it is not clear that this averaging process could maintain adequate uniformity at the target if there were any significant amount of aberration in the incident laser beam. The Fresnel number requirement would be less severe if high power apodization were applied to the edges of each step: one possible technique for achieving this is currently under development.[29] Thus. the quasi near-field version of ISI may become a viable alternative that would be particularly useful for flat foil acceleration experiments. The remaining issues would then be the limited depth of focus [approximately the spot size $\times (F/\text{number})$]. and the cost and complexity of the apodized steps.

This paper presents a theoretical description of the conventional (far-field) version of ISI: "flat topped" ISI will be the subject of a later paper. Section II describes the ISI configuration in greater detail. and calculates the ideal profiles in the single-focus and quadrature modes described above. Section III examines nonuniformities in the average intensity and ablation pressure due to residual interference among the beamlets within finite averaging times. These results are generalized to a partial ISI configuration, where beamlets at larger crossing angles are allowed to remain mutually coherent throughout the pulse. Because the resulting interference pattern will contain only high spatial frequencies. which can presumably be smoothed out by thermal diffusion. partial ISI may be one possible way to accommodate a very large number of beamlets without significantly affecting the temporal behavior of the pulse. Section IV examines the perturbing effects of laser aberration and beamlet divergence on the ISI profile. Section V shows numerical simulations comparing ISI results (averaged over times $\tau = 100 t_c$) with those obtained by ordinary quasi near-field illumination and by the RPS technique. In Sec. VI. we present some recent 2D numerical simulations indicating that ISI operation suppresses filamentation in the underdense plasma. Finally. Sec. VII reviews these results, along with those of recent target interaction experiments using ISI. and briefly discusses a promising new technique for implementing ISI without using echelons.[31]

2

II. ISI CONFIGURATION

Consider a collimated laser output beam propagating along the $+z$ direction. Its instantaneous field amplitude at point $x = (x,y)$ within the transverse plane $z = z_L$ can be written in the form

$$E_L(x,t) = bA(x) F(t) e^{-i\omega t}. \tag{2.1}$$

where the complex amplitudes $A(x)$ and $F(t)$ describe the transverse spatial structure (e.g., due to beam aberration) and the temporal dependence, respectively, and b is a constant to be specified later. For a broadband Q-switched pulse, where $\Delta\nu \gg 1/t_{pulse}$, $F(t)$ is well approximated by a quasi-stationary stochastic variable. Its correlation function $F(t + \bar{t}) F^*(t)$ will exhibit a smooth, localized $\bar{t}$-dependence

$$F(t + \bar{t}) F^*(t) = |F(t)|^2 \gamma(\bar{t}). \tag{2.2a}$$

where $\gamma(0) = 1$ and

$$\gamma(\bar{t}) \to 0 \quad \text{for} \quad |\bar{t}| > t_c = 1/\Delta\nu. \tag{2.2b}$$

while the mean square amplitude $|F(t)|^2$ describes the slow temporal behavior of the average intensity over intervals $\sim t_{pulse} \gg t_c$. For any quantity $G(t) = G(F(t))$, the brackets $G(t)$ denote an ensemble average, which is equivalent to the time average

$$G(t)_\tau = \int_t^{t+\tau} G(t') \frac{dt'}{\tau}$$

over interval τ in the limit where $t_c/\tau \to 0$ and $\tau \ll t_{pulse}$. The effects due to averaging each member of the ensemble over a finite number of coherence times will be considered in Sec. III.

An orthogonal pair of echelon structures, each having $N_S \gg 1$ steps of width D_1, slices the beam into an $N_S \times N_S$ array of square beamlets. (If the incident beam is circular, then only $\pi N_S^2/4$ of those beamlets will contain any appreciable energy.) The nth beamlet, which is defined by the two-dimensional vector $\mathbf{n} = (n_x, n_y)$ with n_x and n_y ranging over $1, 2, \ldots, N_S$, is centered at position $x_n = (x_n, y_n)$, where

$$x_n = \left[n_x - \frac{1}{2}(N_S + 1) \right] D_1, \quad y_n = \left[n_y - \frac{1}{2}(N_S + 1) \right] D_1. \tag{2.3}$$

and delayed by time t_n. The total field amplitude can thus be written as the two-dimensional summation

$$E_S(x,t) = b\sum_n u\left[\frac{x - x_n}{D_1} \right] u\left[\frac{y - y_n}{D_1} \right] F(t - t_n) A(x) \exp\left[ik\beta_n \cdot (x - x_n) - i\omega(t - t_n) \right] \tag{2.4a}$$

$$= b\sum_n u\left[\frac{x - x_n}{D_1} \right] u\left[\frac{y - y_n}{D_1} \right] [A_n + (x - x_n) \cdot (\nabla_\perp A)_n$$

$$+ \frac{1}{2} (x - x_n)(x - x_n) : (\nabla_\perp \nabla_\perp A)_n] F(t - t_n) \exp\left[ik\beta_n \cdot (x - x_n) - i\omega t + i\varphi_n \right]. \tag{2.4b}$$

where $k = 2\pi/\lambda$, $u(x)$ is a "top hat" function equal to 1 for $|x| \leq 1/2$ but zero otherwise, $\varphi_n = \omega t_n$ and β_n are, respectively, the phase shifts and deflection angles imposed upon the beamlets by the echelon steps, and $(\ )_n$ means that the enclosed quantity is to be evaluated at x_n. The second order

3

expansion (2.4b) assumes that $A(x)$ varies slowly across each beamlet, with the transverse gradient terms $(\nabla_\perp A)_n$ and $(\nabla_\perp \nabla_\perp A)_n$ describing the incident beam aberration. For the unaberrated terms, we can specify the normalization

$$\sum_n |A_n|^2 = 1 \tag{2.5}$$

without any loss of generality. No attempt is made (nor should be made) to control the optical path delays ct_n to tolerances of order λ, so the phase shifts φ_n are assumed to be mutually independent and randomly distributed between 0 and 2π. The angular deflections β_n are allowed up to $2N_S$ independent adjustments; however, the most useful combinations appear to be either $\beta_n = 0$ for all n (single-focus configuration) or β_n alternating among the values $(\beta,\beta),(\beta,-\beta),(-\beta,\beta),(-\beta,-\beta)$ for the quadrature configuration.

A single lens of focal length f now superimposes the beamlets at a target plane located a short distance $z(<<f)$ in front of the focal point. The complex amplitude at this plane is found by substituting expression (2.4b) into the diffraction integral:[30]

$$E(x,z,t) = \frac{k}{2\pi(f-z)} \int d^2x' \, E_S(x',t) \exp\left[i \frac{k|x'-x|^2}{2(f-z)} - i \frac{k|x'|^2}{2f} \right] \tag{2.6a}$$

$$\approx \frac{k\,b\,\exp[i\chi(x,z,t)]}{2\pi(f-z)} \sum_n F(t-t_n) \exp\left[i\phi'_n(z) - i \frac{kx_n \cdot x}{f-z} \right]$$

$$\times \int_{-D/2}^{D/2} d\xi_x \int_{-D/2}^{D/2} d\xi_y \left[A_n + (\nabla_\perp A)_n \cdot \xi + \frac{1}{2}(\nabla_\perp \nabla_\perp A)_n : \xi\xi \right]$$

$$\times \exp\left\{ -i\frac{k}{f-z}\left[x - \frac{z}{f} x_n - (f-z)\beta_n \right] \cdot \xi + i \frac{z}{2f} \frac{k|\xi|^2}{f-z} \right\}, \tag{2.6b}$$

where $\chi(x,z,t) \equiv k(f-z) - \omega t + k|x|^2/2(f-z)$, and

$$\phi'_n(z) \equiv \varphi_n + kz|x_n|^2/2f(f-z)$$

is a random phase factor. In writing expression (2.6), we have ignored the propagation distances l_n between the echelon steps and the focusing lens. This is justified as long as the target lies in the quasi far-field of the beamlets; i.e., $|z|$ must remain small in comparison to the beamlet focal depth:

$$|z| << 2\lambda f^2/D_1^2 \tag{2.7}$$

Expression (2.6) then takes advantage of the fact that the far-field amplitudes are independent of l_n, except for small phase curvature terms $kl_n|x|^2/2f^2$.[30] The resulting phase differences $k(l_n - l_{n'})|x|^2/2f^2$ between beamlets are negligible, so these terms can be removed from the summations and incorporated into $\chi(x,z,t)$. Because $|\xi| \le D_1/2^{1/2}$, the $|\xi|^2$ term in the exponential of (2.6b) can be ignored as long as condition (2.7) is satisfied. One then obtains

$$E(x,z,t) = \frac{D_1 b \, \exp[i\chi(x,z,t)]}{a} \sum_n F(t-t_n) \exp\left[i\phi'_n(z) - i \frac{kx_n \cdot x}{f-z} \right]$$

$$\times \left[A_n + \left[\frac{f-z}{-ik} \right] (\nabla_\perp A)_n \cdot \nabla_\perp \right.$$

$$\left. + \frac{1}{2} \left[\frac{f-z}{-ik} \right]^2 (\nabla_\perp \nabla_\perp A)_n : \nabla_\perp \nabla_\perp \right] \text{sinc} \left[\pi \frac{x - (z/f) x_n - (f-z)\beta_n}{a} \right]. \tag{2.8}$$

where

$$\text{sinc}(\theta) \equiv \frac{\sin \theta_x}{\theta_x} \frac{\sin \theta_y}{\theta_y} \tag{2.9}$$

and

$$a \equiv (f-z)\lambda/D_1 \simeq f\lambda/D_1 \tag{2.10}$$

are, respectively, the functional form and effective width of the far-field diffraction pattern due to a single unaberrated beamlet of width D_1. The condition required for negligible separation of the beamlets due to their angular divergence is $|x_n| |z| /fa << 1$, or in terms of the F/number f/D of the total aperture $D = N_S D_1$,

$$f/D >> z/2a. \tag{2.11}$$

The largest defocusing $|z|_{max}$ that would be required in a spherical illumination geometry would be the pellet radius $=a$; hence, condition (2.11) can be adequately satisfied by using high F/number optics. Finally, we note that the far-field condition (2.7) can be rewritten as $f/D_1 >> |z|/2a$, and hence follows immediately from (2.11) because $D/D_1 = N_S > 1$.

Returning to Eq. (2.8), we expand the sinc function up to second order in $x_n z/f a$, approximate $f - z \simeq f$, and finally specify $b \equiv (8\pi/cD_1^2)^{1/2}$:

$$E(\mathbf{x},z,t) = \left[\frac{8\pi}{ca^2} \right]^{1/2} \exp[i\chi(\mathbf{x},z,t)] \sum_n F(t - t_n) \exp \left[i\phi'_n(z) - i \frac{k \mathbf{x}_n \cdot \mathbf{x}}{f} \right]$$

$$\times \left\{ A_n + \left[i \frac{f}{k} (\nabla_\perp A)_n - \frac{z}{f} \mathbf{x}_n A_n \right] \cdot \nabla_\perp + \frac{1}{2} \left[-(\frac{f}{k})^2 (\nabla_\perp \nabla_\perp A)_n + (\frac{z}{f})^2 \mathbf{x}_n \mathbf{x}_n A_n \right. \right.$$

$$\left. \left. - 2i \frac{z}{f} \frac{f}{k} \mathbf{x}_n (\nabla_\perp A)_n \right] : \nabla_\perp \nabla_\perp \right\} \text{sinc} \left[\pi \frac{x - f\beta_n}{a} \right] \tag{2.12}$$

Expression (2.12) contains all of the information needed to generate not only the ideal ISI profiles, but also the deviations arising from multi-beamlet interference, aberration, and beamlet divergence effects.

To complete this section, we evaluate the ideal ISI profiles for the single-focus (i.e. complete overlap) and quadrature configurations described previously. ISI generally requires all of the beamlets to be mutually incoherent; i.e., the correlation function defined in (2.2) must satisfy

$$\gamma(t_n - t_{n'}) = \delta_{n,n'} \tag{2.13}$$

In the scheme proposed here, this condition is achieved by choosing the incremental delays Δt to satisfy

$$\Delta t > t_c = 1/\Delta\nu \tag{2.14}$$

for all n. [A factor $\Delta t/t_c \approx 1.5$ will usually be sufficient to ensure that (2.13) is well satisfied if $\Delta\nu \simeq \Delta\nu(FWHM)$.] The ideal profiles are then found from expression (2.12) by applying (2.13) to the ensemble-averaged intensity $I(\mathbf{x},z,t)) = (c/8\pi)\langle|E(\mathbf{x},z,t)|^2\rangle$, and discarding the aberration and beamlet divergence terms. For the complete overlap configuration (all $\beta_n = 0$) one obtains

$$I^{(0)}(\mathbf{x},t) = (1/a^2)\ P_0(t)\ S(\pi x/a) \tag{2.15}$$

where

$$P_0(t) = \sum_n |F(t - t_n)|^2\ |A_n|^2 \tag{2.16}$$

is the ensemble-average of the total power, and

$$S(\boldsymbol{\theta}) = \mathrm{sinc}^2(\boldsymbol{\theta}) = \left[\frac{\sin\theta_x}{\theta_x}\ \frac{\sin\theta_y}{\theta_y}\right]^2 \tag{2.17}$$

is the diffraction profile of a single beamlet. Approximately 82% of the incident energy is contained in the central lobe of $S(\pi x/a)$, as defined by $-a \le x, y \le a$. The quadrature configuration corresponds to $\hat{x}\cdot\beta_n = +\beta(-\beta)$ for even (odd) values of n_x and $\hat{y}\cdot\beta_n = +\beta\ (-\beta)$ for even (odd) values of n_y. This gives

$$I^{(Q)}(\mathbf{x},t) = \frac{1}{a^2}\sum_{\mu,\nu} P_0^{\mu\nu}(t)\ S\left[\pi\frac{x - \mu\delta a}{a},\ \pi\frac{y - \nu\delta a}{a}\right] \tag{2.18}$$

where $\delta a = f\beta$ is the focal spot offset, μ and ν both assume the values ± 1, and the quantities

$$P_0^{-+}(t) = \sum_n^{(e)}\sum_n^{(e)} |F(t - t_n)|^2\ |A_n|^2, \qquad P_0^{--}(t) = \sum_n^{(e)}\sum_n^{(o)} |F(t - t_n)|^2\ |A_n|^2,\ \text{etc.} \tag{2.19}$$

refer to summations over the even (e) and odd (o) steps. The optimum value of $\delta a/a$ depends on the specific target application. For the broadest possible flat-topped profile, as shown in Fig. 2b, the optimum choice would be $\delta a = 0.43a$; to optimize the illumination uniformity and coupling in a multi-beam spherical geometry,[18,19] the best choice centers around $\delta a \approx 0.22a$.

In order to avoid significant temporal broadening effects due to the echelons, the total differential delay should remain short in comparison to the pulsewidth; i.e.,

$$t_{max} - t_{min} \approx N_S^2\ \Delta t \ll t_{pulse}. \tag{2.20}$$

[The combination of this criterion and condition (2.14) thus places restrictions on the maximum number of steps and the minimum optical bandwidth.] If (2.20) is applicable, then $|F(t - t_n)|^2$ may be removed from the summations in (2.16) and (2.19), which are then subject to the normalization condition (2.5); e.g., the total average power can be written as

$$P_0(t) = |F(t)|^2 \tag{2.21}$$

In the quadrature configuration, the summations will satisfy the condition $P_0^{++}(t) + P_0^{--}(t) + P_0^{-+}(t) + P_0^{+-}(t) = P_0(t)$; thus, in the ideal case where these summations can be exactly balanced, the profile becomes

$$I^{(Q)}(\mathbf{x},t) = (1/a^2)\ P_0(t)\ Q(\pi x/a, \delta a/a). \tag{2.22}$$

6

where

$$Q(\pi x/a, \delta a/a) = \frac{1}{4} \sum_\mu \sum_\nu S \left(\pi \frac{\tau - \mu \delta a}{a}, \pi \frac{\nu - \nu \delta a}{a} \right) \tag{2.23}$$

The $S(\pi x/a)$ and $Q(\pi x/a, \delta a/a)$ profiles are compared in Fig. 2.

III. NONUNIFORMITIES DUE TO RESIDUAL INTERFERENCE

The target responds to quantities, such as intensity or ablation pressure, averaged over some finite number τ/t_c of coherence times. Unlike ensemble averages, these finite time averages will retain small nonuniformities due to residual interference among the beamlets, even if the beamlets are mutually incoherent. This section will examine those nonuniformities in the limit where perturbations due to aberration and beamlet divergence are negligible. For simplicity, we consider only the complete overlap configuration; the quadrature configuration will produce similar results for the cases of interest where $\delta a < 0.4a$. The amplitude $E(x,t)$ can then be approximated by the zeroth order term in Eq. (2.12), with $\beta_n = 0$. Thus, the time-averaged intensity profile can be written as the multimode expansion

$$I(x,t)_\tau = (c/8\pi) \langle E(x,t)^2 \rangle_\tau$$

$$= \frac{1}{a^2} S \left(\pi \frac{x}{a} \right) \sum_m P_m(t)_\tau \exp(i K_m \cdot x), \tag{3.1}$$

where $S(\pi x/a)$ is the ideal diffraction envelope defined in Eq. (2.17), and

$$P_m(t)_\tau = \sum_n A_n A^*_{n-m} \exp(i\phi'_n - i\phi'_{n+m}) \int_t^{t+\tau} F(t' - t_n) F^*(t' - t_{n-m}) \frac{dt'}{\tau}. \tag{3.2a}$$

$$K_m = k(x_{n+m} - x_n)/f = mkD_1/f = (2\pi/a)m = m \Delta K \tag{3.2b}$$

are, respectively, the complex amplitudes and spatial frequencies of the transverse modes. The $m = 0$ amplitude $P_0(t)_\tau = \langle F(t)^2 \rangle_\tau$ is the time average of the total power, so (3.2a) represents a straightforward generalization of (2.16). All of the $m \neq 0$ modes, which describe the interference pattern, are statistically independent, except for the constraint $P_{-m}(t)_\tau = P_m(t)_\tau^*$ required to ensure that $I(x,t)_\tau$ is real.

The actual target acceleration is determined by the average ablation pressure $p(x,t)_\tau$, rather than the intensity itself. In general, $p(x,t)_\tau$ can be related to the instantaneous intensity $I(x,t)$ by a space-time convolution over the conduction zone between the ablation surface and absorption region. This relationship will depend upon the detailed hydrodynamic behavior within that zone, and upon the optical wavelength, average irradiance level, and other parameters that also affect the absorption in the underdense plasma.

To a good approximation, one can ignore the temporal convolution and relate the time-averaged pressure $p(x,t)_\tau$ to a spatial convolution over the time-averaged intensity $I(x,t)_\tau$ in the limit where τ satisfies the condition

$$t_{pulse} > t_{hydro} \geq \tau \gg t_s, t_{th}, \tag{3.3}$$

where t_s and t_{th} are, respectively, the ion-acoustic transit and thermal diffusion times across the conduction zone. These times are given by the approximate expressions

7

$$t_s \approx d/c_s \quad , \quad t_{th} \approx d^2/v_e^2 \tau_{ei} \quad ,$$

where d is the effective width of the conduction zone, $c_s = 9.8 \times 10^5 \, (Z/A)^{1/2} \, [T_e(eV)]^{1/2}$ (with atomic number A and charge state Z) is the ion-acoustic velocity in cm/sec, $v_e = 4.2 \times 10^7 \, [T_e(eV)]^{1/2}$ is the electron thermal speed, $\tau_{ei} = 3.4 \times 10^5 \, [T_e(eV)]^{3/2}/n_e \ln \Lambda$ is the electron-ion collision time[31] in sec, n_e is the electron number density, and $\ln \Lambda$ is the Coulomb logarithm. For recent NRL planar-target experiments using 527 nm, 2 ns pulses at intensities $\sim 10^{13} - 10^{14} \, W/cm^2$,[20] we estimate $T_e \sim 500 \, eV$, $d \sim 50 \, \mu m$,[5] and $n_e \sim 10^{22} \, cm^{-3}$; these parameters then yield $t_s \sim 320$ ps and $t_{th} \sim 360$ ps. Condition (3.3) is thus reasonably well-satisfied as long as the gross hydrodynamic response of the target occurs on nanosecond time scales. A similar result is expected for reactor-sized targets operating at shorter optical wavelengths, longer pulsewidths, and higher intensities. For example, for a possible high gain pellet driven by a few MJ, 1/4 μm laser with a 5-10 ns pulse at 5×10^{14} W cm^2, we estimate $T_e \sim 750 \, eV$, $d \sim 20 - 50 \, \mu m$, and $n_e \sim 4 \times 10^{22} \, cm^{-3}$; this gives $t_s \sim 100 - 250$ ps and $t_{th} \sim 80 - 500$ ps.

The spatial convolution over $I(x,t)$, is approximated here by using the heuristic "cloudy day" model[1,2] to account for thermal smoothing effects within the conduction zone. If $\tilde{p}(K,t)$, and $\tilde{I}(K,t)$, are the transverse spatial Fourier transforms of $p(x,t)$, and $I(x,t)$, respectively, then the cloudy day model provides the simple result

$$\tilde{p}(K,t) = C \, \tilde{I}(K,t) \, \exp(-|K|d) \tag{3.4}$$

where C is a constant. Taking the Fourier transform of Eq. (3.1), and recalling definition (2.17), one obtains

$$\tilde{p}(K,t) = C' \sum_m \tilde{S}(K - K_m) \, P_m(t) \, \exp(-|K|d) \tag{3.5}$$

where $C' = C/a^2$, and

$$\tilde{S}(K) = \int d^2 r \, S(\pi \frac{r}{a}) \exp(-i \, K \cdot r)$$

$$= \begin{cases} (1 - |K_x|/\Delta K)(1 - |K_y|/\Delta K)a^2 & \text{for } K_x \text{ and } K_y \leq \Delta K \\ 0 & \text{for } K_x \text{ or } K_y > \Delta K \end{cases}$$

is a triangular function whose effective width $\Delta K = 2\pi/a = kD_l/f$ is the intermode spacing. [See Eq. (3.2b).]

We are primarily interested in focal spot diameters $(\sim a)$ that are large in comparison to the width of the conduction zone, specifically the case where

$$\Delta Kd = 2\pi \, d/a < 1 \tag{3.6}$$

Expression (3.5) is therefore well-approximated by

$$\tilde{p}(K,t), \approx C' \sum_m \tilde{S}(K - K_m) \, P_m(t), \exp(-|K_m|d),$$

which transforms back to

$$p(x,t), \approx C' S(\pi \frac{x}{a}) \sum_m P_m(t), \exp(-|K_m|d) \exp(i \, K_m \cdot x). \tag{3.7}$$

Comparing this result to expression (3.1), we see that thermal smoothing tends to filter out the higher spatial frequency modes arising from the interference, but has little effect on the diffraction envelope $S(\pi x/a)$.

In the narrowband limit where t_c exceeds the total time delay $t_{max} - t_{min} = N_S^2 \Delta t$, the beamlets would remain mutually coherent. This limit corresponds to the RPS technique.[22,23] The amplitudes $P_m(t)_\tau$ retain large randomly-phased contributions for all $m \neq 0$, in addition to the $m = 0$ term $P_0(t)_\tau = |F(t)|^2_\tau$; hence the average intensity profile (3.1) would consist of a stationary but random multimode interference pattern modulated by the smooth $S(\pi x/a)$ envelope, as illustrated in Fig. 1. Similar considerations apply to the ablation pressure profile (3.7), except that the higher spatial frequency components of the interference pattern are suppressed by the $\exp(-|K_m|d)$ factors. This filtering effect thus provides the primary basis for the RPS technique. In the following paragraphs, we will derive approximate expressions for the RMS mode amplitude of the nonuniform time-averaged intensity and ablation pressure. These expressions can be used to evaluate the standard deviations of the interference nonuniformities for both the narrowband and broadband cases.

A. Complete ISI Operation

For complete ISI operation, $\Delta \nu$ must be broad enough to satisfy conditions (2.14) and (2.20), thus ensuring mutual incoherence for all of the beamlets. The $m \neq 0$ components of $J_m(t)_\tau$ will then decrease in relation to $J_0(t)_\tau$ as t_c/τ decreases; i.e., expressions (3.1) and (3.7) will become dominated by the $S(\pi x/a)$ profile as the interference structure fades away. In the ensemble limit where $t_c/\tau \to 0$, expressions (3.2a), (2.13), and (2.5) yield

$$P_m(t)_\tau \to \langle P_m(t) \rangle_\tau = \delta_{m,0} \langle |F(t)|^2 \rangle_\tau,\qquad (3.8)$$

and both $\langle I(x,t)\rangle_\tau$ and $\langle p(x,t)\rangle_\tau$ [as given by the approximation (3.7)] reduce to the exact $S(\pi x/a)$ profile. The double average in (3.8) allows an averaging over the slow nonrandom variation of $P_0(t)$ in cases where τ could become a non-negligible fraction of t_{pulse}.

The relative magnitude of the interference components of $I(x,t)_\tau$ and $p(x,t)_\tau$ can be quantified by comparing the RMS mode amplitudes for $m \neq 0$ to that of the $DC(m = 0)$ component. Expressions (3.1) and (3.7) suggest the most appropriate definitions are (for $m \neq 0$)

$$\sigma_I(m) \equiv \langle |P_m(t)_\tau|^2 \rangle^{1/2} / \langle P_0(t) \rangle_\tau^{1/2}\qquad (3.9a)$$

$$\sigma_p(m) \equiv \langle |P_m(t)_\tau|^2 \rangle^{1/2} \exp(-|K_m|d)/\langle P_0(t)\rangle_\tau^{1/2} = \sigma_I(m)\exp(-|m|\,\Delta Kd)\qquad (3.9b)$$

where the $\langle\rangle$ brackets again denote an ensemble average, and [recalling (3.2b)] $\Delta K = k\, D_1/f = 2\pi/a$. The total RMS nonuniformities due to all of the statistically independent $m \neq 0$ modes are then evaluated from the vector sums

$$\sigma_I = \left[\sum_{m \neq 0} \sigma_I^2(m)\right]^{1/2}, \qquad \sigma_p = \left[\sum_{m \neq 0} \sigma_p^2(m)\right]^{1/2}\qquad (3.10a,b)$$

A subsequent paragraph will show that $\langle P_0(t)\rangle_\tau^{1/2} \simeq P_0(t)_\tau$; thus, expressions (3.10a,b) may be regarded to a good approximation as the standard deviations of the spatial nonuniformities.

From expression (3.2), we obtain

$$| P_m(t) |_\tau^2 = \sum_n \sum_{n'} A_n A^*_{n+m} A^*_{n'} A_{n'+m} \exp\left[i\left(\phi'_n - \phi'_{n+m} - \phi'_{n'} + \phi'_{n'+m}\right)\right]$$

$$\times \int_t^{t+\tau} \frac{dt'}{\tau} \int_t^{t+\tau} \frac{dt''}{\tau} F(t'-t_n) F^*(t'-t_{n+m}) F^*(t''-t_{n'}) F(t''-t_{n'+m}) \quad (3.11)$$

for all values of m, including m = 0. We now assume that the broadband light is sufficiently chaotic to satisfy Gaussian statistics, thus allowing the factorization[32]

$$F(t'-t_n) F^*(t'-t_{n+m}) F^*(t''-t_{n'}) F(t''-t_{n'+m})$$

$$= \overline{F(t'-t_n) F^*(t'-t_{n+m})} \; \overline{F^*(t''-t_{n'}) F(t''-t_{n'+m})}$$

$$+ \overline{F(t'-t_n) F^*(t''-t_{n'})} \; \overline{F^*(t'-t_{n+m}) F(t''-t_{n'+m})} . \quad (3.12)$$

Temporal mode locking behavior due to "instantaneous" nonlinear effects, such as self-focusing or harmonic conversion, will invariably have some effect on the statistics. However, the Gaussian model is expected to remain a reasonable approximation as long as the number of temporal modes t_{pulse}/t_c (= $\Delta\nu t_{pulse}$) remains large and the average nonlinear phase shift does not exceed 2π by a large amount. Substituting Eq. (3.12) into (3.11) and recalling expression (2.2a) and condition (2.20), one obtains

$$\langle |P_m(t))_\tau|^2 \rangle = \int_t^{t+\tau} \frac{dt'}{\tau} \; |F(t')|^2 \int_t^{t+\tau} \frac{dt''}{\tau} \; |F(t'')|^2$$

$$\times \sum_n \sum_{n'} A_n A^*_{n+m} A^*_{n'} A_{n'+m} \exp\left[i\left(\phi'_n - \phi'_{n+m} - \phi'_{n'} + \phi'_{n'+m}\right)\right]$$

$$\times \left[\gamma(t_{n+m} - t_n)\,\gamma^*(t_{n'+m} - t_{n'}) + \gamma(t'-t'' - t_n + t_{n'})\,\gamma^*(t'-t'' - t_{n+m} + t_{n'+m})\right] \quad (3.13)$$

Equation (3.13) gives for the m = 0 term [recall the normalization (2.5)]

$$\langle P_0(t)_\tau^2 \rangle = \int_t^{t+\tau} \frac{dt'}{\tau} \; |F(t')|^2 \int_t^{t+\tau} \frac{dt''}{\tau} \; |F(t'')|^2$$

$$\times \left[1 + \sum_n \sum_{n'} |A_n|^2 |A_{n'}|^2 |\gamma(t'-t'' - t_n + t_{n'})|^2\right] . \quad (3.14)$$

The second term within the square brackets is nonvanishing only when $t' - t'' - t_n + t_{n'} \approx 0$; hence, if condition (2.20) is satisfied, one can approximate $|F(t')|^2$ by $|F(t'')|^2$ when evaluating the contribution due to this term. In the limit where the total time delay $N_S^2 \Delta t$ satisfies additional criterion $N_S^2 \Delta t << \tau$, condition $t' - t'' - t_n + t_{n'} = 0$ can be attained for all n and n' over most of the $(t, t + \tau)$ interval. The time integrals will then be approximately independent of n and n', so the summations can be evaluated immediately with the aid of Eq. (2.5). Thus,

$$\langle P_0(t)_\tau^2 \rangle \approx \langle |F(t)|^2 \rangle_\tau^2 + \langle |F(t)|^2 \rangle^2 \, \gamma_{RMS}^2 \, t_c/\tau .$$

where $\langle |F(t)|^2 \rangle$ varies negligibly within times $\sim t_c << \tau$, and

$$\gamma_{RMS} = \left[\int_{-\infty}^{\infty} \frac{dt}{t_c} \; |\gamma(t)|^2\right]^{1/2} \approx 1 \quad (3.15)$$

10

is a constant. In the opposite limit where $\tau << N_S^2 \Delta t$, the second term of (3.14) becomes comparable to

$$|F(t)|^{2,2}_\tau \sum_n |A_n|^4 \sim |F(t)|^{2,2}_\tau / N_S^2,$$

which is again small as long as $N_S^2 >> 1$. Recalling expression (3.8), one thus obtains the expected result

$$\overline{P_0(t)^2_\tau} \gtrsim \overline{|F(t)|^2}^2_\tau = \overline{P_0(t)_\tau}^2 \qquad (3.16)$$

in all cases. The standard deviation in the case where $\tau > N_S^2 \Delta t$ is approximately

$$\sigma_0 \equiv \left[\overline{P_0(t)^2_\tau} - \overline{P_0(t)_\tau}^2 \right]^{1/2} / \overline{P_0(t)_\tau} \lesssim \gamma_{RMS} (t_c/\tau)^{1/2} < 1/N_S, \qquad (3.17)$$

assuming that τ is sufficiently short in comparison to t_{pulse} that the slowly-varying quantity $|F(t)|^2$ satisfies $\overline{(|F(t)|^{2})^2}^{1/2}_\tau \simeq \overline{|F(t)|^2}_\tau$. In contrast to Eqs. (3.9) and (3.10), this quantity measures temporal fluctuations of the entire profile amplitude, rather than spatial nonuniformities.

For $m \neq 0$, expression (2.13) eliminates the $\gamma(t_{n+m}-t_n)$ terms in Eq. (3.13), and the random phase factors $\phi'_n - \phi'_{n+m} - \phi'_{n'} + \phi'_{n'+m}$ ensure that only those contributions with $n' = n$ will add coherently in the second set of terms. Equation (3.13) then reduces to the result

$$\langle |\langle P_m(t) \rangle_\tau |^2 \rangle = \langle (|F(t)|^2)^2 \rangle_\tau \gamma^2_{RMS} \frac{t_c}{\tau} \sum_n |A_n|^2 |A_{n+m}|^2. \qquad (3.18)$$

Substituting expressions (3.18) and (3.16) into (3.9) and (3.10), while again assuming $t_c << \tau << t_{pulse}$, one obtains the general results for $m \neq 0$

$$\sigma_I(m)/\tilde\sigma_I(m) = \sigma_I/\tilde\sigma_I = \sigma_p(m)/\tilde\sigma_p(m) = \sigma_p/\tilde\sigma_p = \gamma_{RMS}(t_c/\tau)^{1/2}, \qquad (3.19)$$

where the factors

$$\tilde\sigma_I(m) \equiv \left[\sum_n |A_n|^2 |A_{n+m}|^2 \right]^{1/2}, \qquad \tilde\sigma_I \equiv \left[\sum_{m \neq 0} \tilde\sigma_I^2(m) \right]^{1/2} \qquad (3.20a,b)$$

$$\tilde\sigma_p(m) \equiv \tilde\sigma_I(m) \exp(-|m| \Delta Kd), \qquad \tilde\sigma_p \equiv \left[\sum_{m \neq 0} \tilde\sigma_p^2(m) \right]^{1/2} \qquad (3.21a,b)$$

describe the nonuniformities in the narrowband (RPS) limit. Expressions (3.19) and (3.21) show explicitly that two independent mechanisms are combining to smooth the ablation pressure. The thermal diffusion factors $\tilde\sigma_p(m)$ and $\tilde\sigma_p$ filter out the higher spatial frequencies, but have little effect on the longer wavelength modes unless $\Delta Kd \sim 1$. The temporal factor $\gamma_{RMS}(t_c/\tau)^{1/2} \simeq (t_c/\tau)^{1/2}$, which also smooths the irradiation, reduces the *relative* magnitude of the nonuniformities as the number of independent random intensity contributions τ/t_c increases; it has the exact form that one would expect from a random-walk process where the RMS nonuniformities increase as $(\tau/t_c)^{1/2}$, while the average fluence increases as τ/t_c.

Useful approximations to (3.20) and (3.21) can be obtained using the normalization condition (2.5), provided that the laser output beam is not too badly aberrated (e.g., peak/valley spatial intensity variations < 2:1). In the case of a nominally flat-topped circular beam of diameter $D = N_S D_1$, one

11

can aproximate $|A_n|^2$ by the average value $4/\pi N_S^2$ for $|x_n| \leq D/2$, and zero elsewhere. For $N_S \gg 1$, the n summation in (3.20a) is therefore well-approximated by $(4/\pi N_S^2)^2 \bar{S}$, where $\bar{S}$ is the area of the overlap region between two circles of diameter N_S whose centers are separated by distance $|m| \neq 0$; thus, one obtains

$$\tilde{\sigma}_I(\mathbf{m}) = (8^{1/2}/\pi N_S) \left[\pi/2 - \sin^{-1}(|m|/N_s) - (|m|/N_S)(1 - |m|^2/N_S^2)^{1/2} \right]^{1/2}, \quad (3.22)$$

which is plotted in Fig. 4.

The standard deviation of the integrated intensity can be found immediately by combining (3.19) and (3.20a,b) and using the normalization (2.5):

$$\tilde{\sigma}_I = (1 - \sum_{\mathbf{m}} |A_\mathbf{m}|^4)^{1/2} = (1 - 4/\pi N_s^2)^{1/2} \leq 1 \quad (3.23a)$$

$$\sigma_I \leq \gamma_{\text{RMS}} (t_c/\tau)^{1/2} \quad (3.23b)$$

Expression (3.23a) shows that without temporal averaging, the RMS amplitude of the irradiance nonuniformities remains nearly independent of the number of steps N_S, and is comparable to the DC term. By increasing N_S, one merely shifts the spectrum to higher spatial frequencies, without significantly affecting the total energy in the interference pattern.

The standard deviation of the ablation pressure can be approximated by substituting expression (3.22) into Eqs. (3.21a,b) and (3.19); thus $\sigma_p = \gamma_{\text{RMS}} (t_c/\tau)^{1/2} \tilde{\sigma}_p$, where the 2D summation

$$\tilde{\sigma}_p = \left\{ \frac{8}{\pi^2 N_S^2} \sum_{\mu \neq 0} \left[\frac{\pi}{2} - \sin^{-1} |\mu| \right. \right.$$

$$\left. \left. - |\mu| (1 - |\mu|^2)^{1/2} \right] \exp(-2\Delta K d N_S |\mu|) \right\}^{1/2}, \quad (\mu = m/N_S \leq 1) \quad (3.24)$$

is plotted vs $\Delta K d N_S$ in Fig. 5. To illustrate these results, we consider the parameters used for the ISI simulations shown in Sec. V; i.e., $\lambda = 527$ nm, $f = 6$ m, $N_S = 16$ steps across the FWHM of the beam, stepwidth $D_1 = 1$ cm, and absorption-ablation distance $d = 50$ μm. One then finds $\Delta K d = (k D_1/f)d \approx 1$ and $\Delta K d N_S \approx 16$, thus giving $\tilde{\sigma}_p = 6.6\%$ from Fig. 5 and $\sigma_p < 0.66\%$ for $\tau > 100 t_c$.

For short wavelengths and high gain targets, where condition (3.6) is well-satisfied (e.g., $\Delta K d = 2\pi d/a \leq 0.5$), Fig. 5 shows that $\tilde{\sigma}_p$ depends essentially on the single variable $\Delta K d N_S$, and follows the simple approximation $\tilde{\sigma}_p \leq 2^{1/2}/\Delta K d N_S$. Thus, for a wide range of conditions applicable to high gain laser fusion, the standard deviation of the ablation pressure can be approximated by

$$\sigma_p \leq \gamma_{\text{RMS}} (t_c/\tau)^{1/2} \tilde{\sigma}_p = \sigma_I \tilde{\sigma}_p \quad (3.25a)$$

$$\tilde{\sigma}_p \leq 2^{1/2}/\Delta K d N_S = a/2^{1/2} \pi d N_S = (\lambda/2^{1/2} \pi d) \cdot (f/D) \quad (3.25b)$$

where $f/D = f/N_S D_1$ is the overall F/number of the beam. As a numerical example, we choose $N_S = 60$ steps/beam, $a = 1.5$ mm, $d = 20$ to 50 μm, coherence time $t_c = 1$ ps, and averaging time $\tau = 1$ ns. (The 1.5 mm would allow pellets up to 2 mm radius with quadrature illumination, and the 20 to 50 μm is an appropriate range of absorption-ablation distances for 1/4 μm light.) The standard deviations for the narrowband and broadband cases are then $\tilde{\sigma}_p \leq 11$ to 28% and $\sigma_p \leq 0.4$ to 0.9%, respectively, and the total F/number is $f/N_S D_1 = a/N_S \lambda = 100$ for $\lambda = 0.25$ μm.

We close this discussion with a caveat concerning the slow residual fluctuations in the ideal ablation pressure

$$p_0(\mathbf{x},t)\rangle_\tau = C' \ P_0(t)\rangle_\tau \ S(\pi x/a) \tag{3.26}$$

due to the $P_0(t)\rangle_\tau$ fluctuations. According to the discussion leading to expression (3.17), the standard deviation σ_0 of $P_0(t)\rangle_\tau$ is the lesser of $(t_c/\tau)^{1/2}$ or $1/N_S$, and can therefore amount to several percent. even for $\tau \sim 1$ nsec. This poses no problem as long as one uses only a single laser beam. In a multi-beam spherical illumination geometry,[6-9,19] however, it could lead to a small illumination imbalance, unless all of the beams exhibit nearly the same random temporal behavior. One can avoid the problem by using a single master oscillator and balancing the net time delays within the different chains as closely as possible (at least to within times $\ll t_s, t_{th}$). This will allow some interference to occur among beamlets arising from different beams; however, the large angles (typically $> 20°$) between these beams insure that the resulting transverse wavelengths will be on the order of microns, and hence too short to cause any problem.

B. Partial ISI Operation

Complete ISI operation may be difficult to implement in a large aperture or highly aberrated laser because the large number of incoherent beamlets that could be required would invalidate condition (2.20). The number of beamlets is determined by the step width D_1, which depends upon the target diameter $\leq 2a = 2\lambda f/D_1$ and the amount of aberration in the laser. For $\lambda < 1/2\ \mu m$, reasonable focal lengths (e.g. $f \leq 30\ m$), and high gain targets of a few mm diameter, one would typically need $D_1 < 1$ cm. With a 100 cm aperture per beam this would require $N_S^2 > 10^4$ beamlets: it would significantly affect the temporal behavior of the pulse, because for $t_c \sim 1$ ps. $N_S^2\ \Delta t > N_S^2\ t_c \sim 10$ ns.

One possible way to avoid this problem is a partial ISI scheme, in which the echelon step sequence would be repeated after every $N < N_S$ steps across the aperture. (e.g., see Fig. 12). Expression (2.13) would then be replaced by the more general condition

$$\gamma(t_n - t_{n'}) = \sum_m \delta_{n,n' - Nm}. \tag{3.27}$$

where (m_x, m_y) range over all positive and negative integers. including zero. Because the repeated steps ($m \neq 0$) remain coherent. they create stationary interference patterns at the target. However. if one chooses N sufficiently large. these patterns will have only high spatial frequencies of magnitude $N\Delta K$, $2^{1/2}N\Delta K$, $2N\Delta K$, etc. and can therefore be smoothed out by thermal diffusion. The relative magnitude of the interference components of $p(\mathbf{x},t)\rangle_\tau$ can again be calculated from (3.9) and (3.10). using expression (3.27) and arguments similar to those presented before. Thus, (3.19) and (3.21) generalize to

$$\sigma_p \leq \left[\gamma_{RMS}^2 \frac{t_c}{\tau} \sum_{m \neq 0} \bar{\sigma}_p^2(m) + \sum_{m \neq 0} \bar{\sigma}_p^2(Nm) \right]^{1/2}. \tag{3.28}$$

where the n summations again extend over all N_S^2 beamlets. The first term within the brackets describes the residual incoherent contributions. and is identical to expression (3.19) and (3.21b): the second describes the contribution of stationary interference patterns due to the repeating steps. If one chose $N = 1$ (corresponding to the random phase case) then the second term would be identical to the thermal smoothing factor (3.21b), and would become dominant for $t_c \ll \tau$. If N is chosen large enough to satisfy the condition $2N\Delta Kd \gg 1$. then the second term becomes negligible and (3.28) reduces to the usual ISI result. Thus, for a large high gain pellet where condition (3.6) is well-satisfied. the standard deviation of the ablation pressure would still be described by (3.25a.b). The ISI configuration recently proposed for the Sirius-M test reactor design[18] provides an instructive

13

numerical example. Here, each 1.2 m aperture (square) beam was divided into a total of $N_S = 240$ steps, which repeat after every 60 steps. With a stepwidth $D_1 = 5$ mm, focal length $f = 30$ m, and wavelength $\lambda = 1/4$ μm, this gives $a = f\lambda/D_1 = 1.5$ mm. Assuming (as before) that $d = 20$ to 50 μm and $\tau/t_c = 1000$, we calculate $\sigma_p \sim 0.1$ to 0.25% from (3.25a,b). The overall F/number of each 1.2 m beam is F/25.

IV. ABERRATION AND BEAMLET DIVERGENCE EFFECTS

This section examines perturbations of the ideal target profile due to laser aberration and beamlet divergence. In order to separate out these effects, the analysis will be carried out in the ensemble-average limit $t_c/\tau \rightarrow 0$, assuming complete ISI operation defined by conditions (2.14) and (2.20). Because the resulting expressions contain no interference terms, and therefore involve only the long scalelength functions such as $S(\pi x/a)$ and its first and second-order gradients, they should apply equally well to the average intensity or the ablation pressure as long as condition (3.6) is satisfied.

A. Completely Overlapped Beamlets

The complete overlap configuration is obtained by setting all $\beta_n \rightarrow 0$ in Eq. (2.12). Applying conditions (2.13) and (2.21) to (2.12), and retaining only perturbation terms up to second order, one finds the average intensity $I(x,z) = (c/8\pi)\langle |E(x,z)|^2 \rangle$:

$$I(x,z) = \frac{P_{0t}}{a^2} \sum_n \left\{ \left[|A_n|^2 - \mathrm{Re}(A_n{}^* \mathbf{B}_n) \cdot \nabla_\perp + \frac{1}{2} \mathbf{B}_n \mathbf{B}_n{}^* : \nabla_\perp \nabla_\perp \right] S\left(\pi \frac{x}{a} \right) \right.$$

$$\left. - \left[\frac{f}{k} \right]^2 \mathrm{sinc} \left[\pi \frac{x}{a} \right] [\mathrm{Re}(A^* \nabla_\perp \nabla_\perp A)_n + (\nabla_\perp A)_n (\nabla_\perp A^*)_n] : \nabla_\perp \nabla_\perp \, \mathrm{sinc} \left[\pi \frac{x}{a} \right] \right\} \quad (4.1)$$

where

$$\mathbf{B}(x) = (f/ik)(\nabla_\perp A) + (z/f)xA . \quad (4.2)$$

[Recall that $(\ )_n$ evaluates the enclosed quantity at point x_n.] The slow temporal variation of $I(x,z,t)$ and $P_0(t)$ (on a scale of t_{pulse}) and the z-dependence of $\mathbf{B}_n(z)$ have been suppressed here in order to simplify the notation. Because $A(x)$ varies slowly across the beamlet width D_1, the 2D summations over n can be approximated by integrals. For example the normalization (2.5) can be replaced by

$$\sum_n |A_n|^2 = \int |A(x)|^2 \frac{d^2x}{D_1^2} = 1 . \quad (4.3)$$

and integration by parts can be used to eliminate the last pair of terms in (4.1); i.e.,

$$\sum_n \mathrm{Re}(A^* \nabla_\perp \nabla_\perp A)_n = \frac{1}{2} \int \frac{d^2x}{D_1^2} (A^* \nabla_\perp \nabla_\perp A + c.c.)$$

$$= - \int \frac{d^2x}{D_1^2} (\nabla_\perp A)(\nabla_\perp A^*) = - \sum_n (\nabla_\perp A)(\nabla_\perp A^*) .$$

Equation (4.1) therefore reduces to

$$I(x,z) = [1 - C_1(z) \cdot \nabla_\perp + \frac{1}{2} C_2(z) : \nabla_\perp \nabla_\perp] I^{(0)}(x) . \quad (4.4)$$

where $I^{(0)}(x) = (P_0/a^2) S(\pi x/a)$ is the ideal target profile defined in Sec. II, and

14

$$C_1(z) = \int \frac{d^2x}{D_1^2} Re(A^*B), \quad C_2(x) = \int \frac{d^2x}{D_1^2} BB^* \qquad (4.5)$$

are the aberration coefficients. These coefficients can be rewritten in terms of the phase $\Phi(x)$ and modulus $|A(x)|$ of the amplitude $A(x)$; i.e.,

$$C_1(z) = \int \frac{d^2x}{D_1^2} |A(x)|^2 [f\theta(x) + \frac{z}{f} x]. \qquad (4.6a)$$

$$C_2(z) = \int \frac{d^2x}{D_1^2} |A(x)|^2 \{[f\theta(x) + \frac{z}{f}x]^2 + [\frac{f}{k}\nabla_\perp \ln|A|]^2\}. \qquad (4.6b)$$

where $\theta(x) \equiv (1/k)\nabla_\perp \Phi(x)$ is the refraction angle acquired by the aberrated wavefront around point x, and the squared vectors $[\quad]^2$ in (4.6b) represent diadic products $[\quad][\quad]$. Expressions (4.6a,b) can be interpreted physically as intensity—weighted averages of the bracketed quantities over the laser aperture.

It is useful to relate $C_1(z)$ and $C_2(z)$ to spatial moments[33] of the coherent (but aberrated) focal distribution $I_C(x,z)$ that the laser would produce without ISI. As shown in the appendix, expression (4.6a) is just the centroid of the coherent beam:

$$C_1(z) = \{x_C\}_z \equiv \int \langle I_C(x,z)\rangle x d^2x / \int \langle I_C(x,z)\rangle d^2x \qquad (4.7)$$

This result can be readily understood in terms of geometrical optics. A ray passing through point x in the laser aperture will intercept the target plane at point $x_C(x) = f\theta(x) + xz/f$; expression (4.6a) then averages all such contributions over the entire laser aperture. For the second moment $\{x_C x_C\}$, which is a measure of the RMS width of $\langle I_C(x,z)\rangle$, geometrical optics would average the diadic $[f\theta(x) + xz/f]^2$ over the laser aperture, thus giving the first set of terms in (4.6b). A more thorough treatment including diffraction yields the complete expression (Appendix)

$$C_2(z) = \{x_C x_C\}_z \equiv \int I_C(x,z) xx d^2x / \int I_C(x,z) d^2x . \qquad (4.8)$$

although the geometrical optics contribution will usually remain dominant in saturated lasers, where most of the aberration resides in the phase.

The aberrated ISI profile (4.4) can now be expressed in terms of the coherent moments:

$$\langle I(x,z)\rangle = [1 - \{x_C\}_z \cdot \nabla_\perp + \frac{1}{2}\{x_C x_C\}_z : \nabla_\perp \nabla_\perp] \langle I^{(0)}(x)\rangle \qquad (4.9)$$

By dividing out the maximum value $I^{(0)}(0)$, one can rewrite this in a dimensionless form suitable for comparing the magnitudes of the perturbation terms; i.e.,

$$\langle I(x,z)\rangle / \langle I^{(0)}(0)\rangle = S(\pi x/a) - \pi(\{x_C\}_z/a) \cdot S'(\pi x/a)$$

$$+ \frac{1}{2}\pi^2(\{x_C x_C\}_z/a^2) : S''(\pi x/a). \qquad (4.10)$$

where

$$S'(\alpha) \equiv \nabla_\alpha S(\alpha), \quad S'' \equiv \nabla_\alpha \nabla_\alpha S(\alpha). \qquad (4.11)$$

15

and $\nabla_\alpha = \partial/\partial\alpha$. The functions $S(\alpha_x,0)$, $S'_x(\alpha_x,0)$, and $S''_{xx}(\alpha_x,0)$ are compared in Fig. 6. Equation (4.9) can also be expressed in an alternative form by expanding $I^{(0)}(x)$ around point $\{x_C\}_z$ and, as usual, retaining terms only up to second order in the gradients; i.e.,

$$I(x,z) \approx [1 + \frac{1}{2}\{\Delta x_C \Delta x_C\}_z : \nabla_\perp \nabla_\perp] I^{(0)}(x - \{x_C\}_z) , \tag{4.12}$$

where

$$\{\Delta x_C \Delta x_C\}_z \equiv \{x_C x_C\}_z - \{x_C\}_z \{x_C\}_z . \tag{4.13}$$

Because $I^{(0)}(x)$ is symmetric around $x = 0$, it is apparent that $\{x_C\}$ also defines the centroid (and hence the alignment) of the ISI profile. A nonzero value of $\{x_C\}_z$ would be of little consequence in a flat foil experiment, where precise alignment is unnecessary. However, in a spherical geometry where each laser beam must be properly centered onto the pellet, $\{x_C\}_z$ should be treated as a perturbation term [c.f. Eq. (4.10)] if it cannot be entirely removed by the alignment system.

If the aberrations are spatially random, one can use a simple statistical model[34] to estimate both the magnitudes and reproducibility of the perturbation amplitudes in Eq. (4.10). This model should provide a reasonable description of perturbations arising from small-scale effects such as turbulence, multiple surface nonuniformities, and residual lens aberrations, which contribute the lion's share of the far-field broadening and are the most difficult to eliminate. Systematic lens aberrations, such as astigmatism in angularly—multiplexed KrF systems,[35,36] can be largely compensated within the laser. Large-scale effects, such as thermal gradients, tend to cause gradual beam steering effects rather than any significant broadening, and can be balanced out in real-time by an automatic alignment system. For simplicity, the model will treat only phase aberration, which is the primary culprit responsible for both beam steering and broadening effects in real lasers. The random phase aberration is characterized by an effective coherence width $s_{ab} < D$ (where D is the laser aperture), over which the RMS phase shift is π. The local refraction angle $\theta(x) = (1/k)\nabla_\perp\Phi(x)$ can then be characterized using a number

$$N_{ab}^2 = (D/s_{ab})^2 > 1 \tag{4.14}$$

of statistically-independent contributions θ_j whose ensemble-average values are $\langle\theta_j\rangle = 0$ (assuming that the laser is properly aligned) and whose RMS amplitudes are

$$\theta_{RMS} \equiv |\theta_j|^{2,1/2} = \pi/ks_{ab} = \lambda/2s_{ab} . \tag{4.15}$$

From Eqs. (4.6a,b) (4.7) and (4.8), one thus obtains for the relevant moments

$$\{x_C\} \approx \frac{f}{N_{ab}^2} \sum_{j=1}^{N_{ab}^2} \theta_j , \qquad \{x_C x_C\} \approx \frac{f^2}{N_{ab}^2} \sum_{j=1}^{N_{ab}^2} \theta_j\theta_j , \tag{4.16a,b}$$

where the subscript z has been dropped in order to simplify the notation.

Combining Eqs. (4.14)-(4.16a) and using the statistical conditions $\langle\theta_j\rangle = 0$ and $\langle\theta_j\cdot\theta_j\rangle = \theta_{RMS}^2 \delta_{ij}$, one obtains the ensemble-average $\langle x_C\rangle = 0$ and the RMS centroid

$$(\{x_C\})_{RMS} \equiv |\{x_C\}|^{2,1/2} \approx f\theta_{RMS}/N_{ab} = f\lambda/2D ; \tag{4.17}$$

i.e., the RMS misalignment due to small scale beam steering effects is approximately half the diffraction-limited far-field width $f\lambda/D$. (This expression probably represents an upper bound on the misalignment because at least some of the contributions to it may be correctable by an automatic

alignment system.) The RMS value of the $S'(\pi x/a)$ coefficient in Eq. (4.10) thus reduces to the simple result

$$R_1 = \pi(|x_C|)_{RMS}/a \approx (\pi/2)f\lambda/Da \qquad (4.18a)$$

$$= \pi/2N_S . \qquad (4.18b)$$

where Eq. (2.10) and the relationship $N_S = D/D_1$ was used to obtain (4.18b). [Note that the criterion specified in Sec. II requires $N_S/N_{ab} = s_{ab}/D_1 >> 1$ (e.g. ≥ 3) to ensure the accuracy of the perturbation expansion (4.10). For the two large-scale ISI examples discussed in Sec. III, where we chose $N_S = 60$ and 240, the respective values of R_1 are 2.5% and 0.6%. It should be noted that expression (4.18a) is also applicable to conventional illumination schemes,[6-8] where a would represent the diameter of the quasi near-field profile at the target. Obviously, aberration-induced beam steering is an issue that can affect all spherical illumination schemes, not just ISI.

The mean value of the second moment $|x_C x_C|$ will reduce to its diagonal elements $|x_C^2| = |y_C^2| = ||x_C|^2|/2$ as long as the aberration is spatially-random. Combining Eqs. (4.14), (4.15) and (4.16b), one obtains for the mean square diameter of the (non-ISI) focal spot

$$4(||x_C|^2|) \approx (2f\theta_{RMS})^2 = (f\lambda/s_{ab})^2 = (f\lambda/D)^2 N_{ab}^2 . \qquad (4.19a)$$

which can be rewritten in the intuitively satisfying form

$$N_{ab} \approx 2(||x_C|^2|)^{1/2}/(f\lambda/D)$$

$$= (\text{RMS diameter}) / (\text{diffraction - limited diameter}). \qquad (4.19b)$$

The effective magnitude of the $S''(\pi x/a)$ coefficient in Eq. (4.10) is then

$$R_2 = (\pi^2/8)4(||x_C|^2|)/a^2$$

$$\approx (\pi^2/8)(N_{ab}D_1/D)^2 = (\pi^2/8)N_{ab}^2/N_S^2 . \qquad (4.20)$$

which tends to broaden the ISI profile, as shown in Fig. 7. If the laser aberration N_{ab} were only a few times diffraction limit, one could virtually eliminate this broadening term without using an excessive number of steps; e.g., a choice of $N_S/N_{ab} > 10$ would reduce R_2 to about 1% or less. However, the high power multistage lasers envisioned as fusion drivers are likely to be heavily aberrated, with typical values $N_{ab} \sim 10$ to 20 for each 30 cm of aperture. It is therefore expected that N_S/N_{ab} will lie in the range of 3 to 5, giving the respective values $R_2 \approx 15\%$ to 5%. The function $S''(\pi x/a)$ is smooth and symmetric (Fig. 6), so a perturbation amplitude of this size will be tolerable as long as it remains reproducible to within $\sim 10\%$. Because of the spatial averaging process inherent in expressions (4.6a,b) one can expect a high degree of reproducibility.

The magnitude ΔR_2 of the non-reproducible part of the perturbation amplitude can be estimated from the RMS deviation

$$\Delta(|x_C|^2) = [(||x_C|^2|^2 - ||x_C|^2|)^2]^{1/2} \qquad (4.21a)$$

$$\approx \frac{f^2}{N_{ab}^2} [\sum_{j=1}^{N_{ab}^2} (|\theta_j|^4 - |\theta_j|^{2\cdot2})]^{1/2} . \qquad (4.21b)$$

17

where expression (4.21b) follows from (4.16b) and the statistical independence of the θ_j contributions. Under chaotic conditions, one can approximate $|\theta_j|^4 - |\theta_j|^{2\cdot 2}$ by θ_{RMS}^4, thereby obtaining $\Delta\{|x_C|^2\} \approx f^2\theta_{RMS}^2/N_{ab}$. The resulting contribution to the perturbation amplitude is then

$$\Delta R_2 = (\pi^2/8)4\Delta\{|x_C|^2\}/a^2$$

$$\approx R_2/N_{ab} = (\pi^2/8)N_{ab}/N_S^2. \tag{4.22}$$

according to (4.14), (4.19a) and (4.20). For the simulations discussed in Sec. V ($N_{ab} \approx 5 \times$ diffraction limit and $N_S = 16$ steps across the FWHM of the beam) one expects $\Delta R_2 \approx 2.4\%$; however, ΔR_2 will be much smaller under the conditions applicable to a fusion driver. For example, a 20 $\times$ diffraction-limited beam in a 30 cm aperture with 60 steps would have $\Delta R_2 \approx 0.7\%$; a 1.2 m compound aperture consisting of a 4 $\times$ 4 array of such beams (i.e., $N_{ab} \approx 80$ and $N_S = 240$) would allow only $\Delta R_2 \approx 0.17\%$.

B. Quadrature Configuration

The above perturbation treatment gives similar results for the effects of phase aberration and beamlet divergence on the quadrature profile, at least for the cases of interest where the offset δa satisfies $\delta a < 0.4a$. Unlike the complete overlap case, however, the quadrature profile $I^{(Q)}(x)$ may be affected by laser intensity nonuniformities even if the usual perturbation terms in Eq. (4.10) were negligible. To examine this effect in greater detail, we rewrite expression (2.18), assume condition (2.20), and recall the normalization $P_0^{++} + P_0^{+-} + P_0^{-+} + P_0^{--} = P_0$:

$$I^{(Q)}(x) = \frac{P_{0,}}{a^2} Q(\pi x/a, \delta a/a) + \sum_{\mu,\nu}\sum_{\mu',\nu'} \frac{P_0^{\mu\nu} - P_0^{\mu'\nu'}}{8a^2}$$

$$\times \left[S\left(\pi\frac{x - \mu\delta a}{a}, \pi\frac{y - \nu\delta a}{a}\right) - S\left(\pi\frac{x - \mu'\delta a}{a}, \pi\frac{y - \nu'\delta a}{a}\right) \right]. \tag{4.23}$$

where $Q(\pi x/a, \delta a/a)$ is the ideal quadrature defined in Eq. (2.23). We now expand the S functions up to second order around $S(\pi x/a)$ (valid for small $\delta a/a$) and combine the $P_0^{\mu\nu}$, $P_0^{\mu'\nu'}$ summations to finally obtain

$$I^{(Q)}(x) \approx \frac{P_{0,}}{a^2} \left\{ Q(\pi x/a, \delta a/a) \right.$$

$$\left. + (\pi\delta a/a)\,[C_x\,S'_x(\pi x/a) + C_y S'_y(\pi x/a)] + (\pi\delta a/a)^2\,C_{xy}\,S''_{xy}(\pi x/a) \right\}. \tag{4.24}$$

where

$$C_x = \left[\overset{(o)}{\sum_{n}} - \overset{(e)}{\sum_{n}}\right]\sum_{n}|A_n|^2, \quad C_y = \sum_{n}\left[\overset{(o)}{\sum_{n}} - \overset{(e)}{\sum_{n}}\right]|A_n|^2, \tag{4.25a,b}$$

$$C_{xy} = \left[\overset{(o)(o)}{\sum_{n}\sum_{n}} + \overset{(e)(e)}{\sum_{n}\sum_{n}} - \overset{(o)(e)}{\sum_{n}\sum_{n}} - \overset{(e)(o)}{\sum_{n}\sum_{n}}\right]|A_n|^2. \tag{4.25c}$$

and the functions $S'(\pi x/a)$, $S''(\pi x/a)$ are defined in Eq. (4.11).

18

One can null out most of the contribution to coefficients (4.25a-c) just by carefully aligning and orienting the echelons within the beam; however, in practical lasers, where the saturated near-field profile varies during the pulse duration (and may not even be completely reproducible from shot-to-shot), the residual contributions should probably be treated as random variables. Each of them would then have the approximate RMS value

$$C_{RMS} = (\tfrac{1}{2}N_S^2)^{1/2}(\Delta|A|^2)_{RMS} \approx (1/2^{1/2}N_S)(\Delta|A|^2)_{RMS}/(|A|^2)_{av} ,$$ (4.26)

where $(|A|^2)_{av} \approx 1/N_S^2$ and $(\Delta|A|^2)_{RMS}$ respectively describe the average and RMS deviation of the intensity across the laser profile. For example, a ratio $(\Delta|A|^2)_{RMS}/(|A|^2)_{av} \approx 0.15$ (corresponding to $\approx$ 2:1 peak/valley variation) would give $C_{RMS} \approx 0.1/N_S$, which gives $C_{RMS} \approx 0.7\%$ for $N_S = 16$ and 0.2% for $N_S = 60$.

V. NUMERICAL SIMULATIONS OF ISI

The beam smoothing behavior of ISI can be clearly illustrated by numerical simulations of the time-averaged intensity and ablation pressure profiles for a planar target. These simulations were carried out for 0.527 μm light by a 3D numerical code (CHAOS), which evaluates the diffraction integral (2.6a) for an incident laser beam of arbitrary aberration, but ignores refraction and filamentation in the underdense plasma. Thermal smoothing effects are modelled by the heuristic "cloudy day" approximation, as defined in expression (3.4), assuming in these examples an effective absorption-ablation distance of $d = 50$ μm. For the simulations shown here, the chaotic temporal behavior of the laser light is modelled by Gaussian statistics. The real and imaginary parts of the complex amplitude $F(t)$ are assigned independent random values with a Gaussian probability distribution, and these values fluctuate randomly from one coherence time to the next. Some of the simulations were also carried out using other statistical distributions, such as random phase with constant intensity; the results indicated that the ISI smoothing should be relatively insensitive to the statistics of the incident light.

Figure 8 illustrates the problem encountered by the conventional illumination scheme.[7,8,10,11] where the target is simply placed in the quasi near-field of the focusing lens. In order to model a saturated laser beam, the incident aberration was chosen to reside primarily in the phase: i.e., the ~20 cm beam had a 5 × D.L. angular spectrum, but only ~30% peak/valley intensity nonuniformities. This was accomplished by choosing the random complex amplitude $A(x)$ to satisfy Gaussian statistics, then attenuating the intensity nonuniformities by replacing the modulus $|A(x)|$ by $|A(x)|^{1/8}$. The overall laser profile was modelled by multiplying the resulting values of $A(x)$ by a hypergaussian envelope $\{\exp[-(2|x|/D)^{10}]\}^{1/2}$. At the target, where the beam has focused down to ≥ 0.5 mm, the irradiance nonuniformities are significantly worse because of the phase aberration in the incident beam.[10,11] Large random nonuniformities are also very evident in the ablation pressure profile, although thermal smoothing has removed the higher spatial frequency components.

Figure 9 models the original version of the RPS technique.[22,23] A pair or reflecting echelons ($N_S = 20, D_1 = 1$ cm) have been inserted into the beam with their alternating steps tilted to produce a quadrature profile at the target plane, which is now located in the far field of a 6 meter lens. (This configuration is similar to the one used in recent NRL experiments with broadband 0.527 μm light.[20]) In this case, however, the bandwidth $\Delta\nu$ is assumed to be sufficiently narrow that all 400 beamlets remain mutually coherent, thus resulting in a complicated interference pattern that remains stationary throughout the pulse. The thermal smoothing mechanism was unable to filter out the lower spatial frequency components in the corresponding ablation pressure. The maximum peak/valley deviation from the ensemble-averaged profile $p(x)$ was found to be 37%, which is consistent with the RMS value $\bar{\sigma}_p = 6.6\%$ calculated in Sec. III. Because the RPS technique allows a smaller stepwidth than ISI, it would be possible to reduce this nonuniformity by increasing the number of steps. [E.g., see Eq. (3.25b).] However, it would also be necessary to either increase the laser aperture $N_S D_1$ or

decrease the focal length f in order to maintain the same spot size a. For example, a tenfold decrease in $\bar{\sigma}_p$ would require $N_S = 200$, which would in turn require F/3 optics.

Figures (10) and (11) show the time-average intensity and ablation pressure profiles for the complete ISI case, in which $\Delta\nu$ is now chosen large enough to ensure mutually-incoherent beamlets. Although the averaging interval $\tau = 100 \, t_c$ was chosen relatively short in this simulation, the quality of the target profiles already shows dramatic improvement over previous results. The residual low amplitude structure on the average intensity profile has been all but completely eliminated from the ablation pressure $p(x)_\tau$. The maximum (peak/valley) deviation from the ideal (ensemble-averaged) pressure $p(x)$ was found to be 2.4%, which is consistent with the RMS value $\sigma_p = 0.66\%$ calculated in Sec. III. On the basis of Eq. (3.25a), we expect the maximum deviation to be $< 1\%$ with averaging times $\tau > 500 t_c$.

Figures 12 and 13 simulate the partial ISI case, where the time delay sequence now repeats after the 10th step; thus steps 1 and 11, 2 and 12, etc remain coherent. The resulting increase in fine scale interference structure (of wavelength $\lambda f / 10 D_1 = 32 \, \mu m$) is clearly evident in the average intensity, and would persist throughout the entire pulse. As a result of thermal smoothing, however, this structure is effectively removed from the ablation pressure; e.g., the corresponding contribution to expression (3.28) is proportional to $\exp(-4\pi N d / a) = \exp(-20)$. The 3.9% peak/valley deviation found here is somewhat larger than in the previous case, but that difference appears to be statistical.

VI. FILAMENTATION SIMULATIONS

The filamentation instability is an important consideration in the use of ISI. Because the hydrodynamic response time for filamentation (typically $\sim$ 100 ps) is much longer than the laser coherence time (about 1 ps), it would appear that filamentation would be easily suppressed by ISI. In addition, random density fluctuations driven by the constantly changing intensity structure would act to diffuse any residual intense spots, and spoil filamentation further.

On the other hand, the smoothing effect of ISI is incomplete on the filamentation-hydrodynamic time scales; time-averaged intensity fluctuations of $\sim$ 10% persist over this period, and may still drive filamentation. Also, there will be short moments during which the local intensity incident on target will be much higher than average. [For Gaussian statistics, the intensity distribution is $(1/\bar{I})\exp(-I/\bar{I})$.] Because filamentation is inherently a nonlinear optical instability, one may argue that these momentary intensity peaks, rather than the time averaged fluctuations, dominate the filamentation behavior. Thus the effect of ISI on light filamentation is not readily discernible from simple arguments.

A numerical code SELFOCT has been developed to simulate thermal and ponderomotive self focusing in laser-plasma interactions, and particularly any filamentation of the light inhomogeneities that may occur under ISI conditions. The code is time dependent and Cartesian in two spatial dimensions. Light propagation is handled by the parabolic wave equation, while the plasma dynamics are calculated by semi-linearized fluid equations combined with flux-limited heat flow.

A. Code Description

Laser propagation in SELFOCT is described by the paraxial WKB approximation to Maxwell's wave equation

$$(c^2 \nabla^2 - \partial^2 / \partial t^2) E = (1 - i\nu_{ei}/\omega)\omega_p^2 E. \qquad (6.1)$$

This equation assumes a quasi-neutral plasma characterized by the local plasma frequency $\omega_p = \omega [n_e(x,z,t)/n_c]^{1/2}$ and electron-ion collision frequency $\nu_{ei} \propto n_e(x,z,t)/T_e^{3/2}(x,z,t)$.[3] One can separate the field variations into fast and slow space-time scales by writing

$$E(x,z,t) = \Psi(x,z,t)\exp\left[i\int_0^z k_0(z')dz' - i\omega t\right]. \tag{6.2}$$

where $\Psi(x,z,t)$ is the slowly-varying complex amplitude, $k_0 = \epsilon_{or}^{1/2}(z)\omega/c$, and $\epsilon_{or} = 1 - n_{eo}(z)/n_c$ is the real part of the dielectric constant determined by the unperturbed steady-state density $n_{eo}(z)$. In the paraxial WKB approximation, $\Psi(x,z,t)$ and $k_0(z)$ remain slowly-varying over spatial scales $\lambda \sim 2\pi/k_0(z)$. Substituting (6.2) into (6.1) and retaining only the first order variations of $\Psi(x,z,t)$ in z and t, one obtains

$$\left[2ik_0\left(\frac{\partial}{\partial z} + \frac{1}{v_g}\frac{\partial}{\partial t}\right) + i\frac{\partial k_0}{\partial z} + \frac{\partial^2}{\partial x^2}\right]\Psi$$

$$= -\frac{\omega^2}{c^2}(\epsilon_r - \epsilon_{or} + i\epsilon_i)\Psi. \tag{6.3}$$

Here, $\epsilon_r(x,z,t) = 1 - n_e(x,z,t)/n_c$ and $\epsilon_i(x,z,t) = v_{ei}(x,z,t)n_e(x,z,t)/n_c\omega$ are, respectively, the real and imaginary parts of the instantaneous plasma dielectric constant, and $v_g(z) = c\epsilon_{or}^{1/2}(z)$ is the group velocity. This equation can be simplified by applying the additional transformation

$$\Psi = \psi\left[\frac{k_0(0)}{k_0(z)}\right]^{1/2}\exp\left[-\frac{\omega}{c}\int_0^z\frac{\epsilon_{oi}(z')}{2\epsilon_{or}^{1/2}(z')}dz'\right]. \tag{6.4}$$

where $\epsilon_{oi}(z) = v_{ei}(z)n_{eo}(z)/n_c\omega$, and rewriting all quantities in terms of the time $\bar{t} = t - z/v_g(z)$. Redefining the axial coordinate as $d\eta = dz/\epsilon_{or}^{1/2}(z)$ and normalizing both spatial coordinates to the optical wavelength $\lambda = 2\pi c/\omega$, one finally arrives at the parabolic equation in canonical form

$$(4\pi i\,\partial/\partial\eta + \partial^2/\partial x^2)\psi(x,z,\bar{t}) = -4\pi^2\left[\epsilon(x,z,\bar{t}) - \epsilon_0(z)\right]\psi(x,z,\bar{t}). \tag{6.5}$$

where $\epsilon = \epsilon_r + i\epsilon_i$ is the complex dielectric constant.

Equation (6.5) is solved using a split-step fast Fourier transform (FFT) technique.[17] To accommodate the FFT technique, the computational mesh must be periodic in x, and this affects the manner in which the incident $(z = 0)$ ISI laser field is numerically constructed. The ISI echelons separate the broadband laser beam into a multitude of mutually-incoherent beamlets, which are then overlapped at the target by the focusing lens. In the SELFOCT code, these overlapping beamlets are approximated by incoherent plane waves propagating at slightly different angles $\theta_n = x_n/f$, where x_n is given by expression (2.3) and $|\theta_n| << 1$. The incident optical field is constructed on a calculational mesh in Fourier k-space, with each plane wave assigned a transverse spatial frequency $k_{xn} = k_0(0)\tan\theta_n \simeq k_0(0)\theta_n$, where $k_0(0) = \omega/c$. Modes are exactly resolvable when $|k_{xn}|X_{len}$ is an integer multiple of 2π, where X_{len} is the transverse width of the mesh; modes that lie between the points on this k-space mesh are assigned to the nearest mesh point. Any modes outside of the resolvable frequency range (i.e., $|k_{xn}|X_{len} < \pi$) are assigned to the $k_x = 0$ (DC) mode. The complex amplitude of each beamlet is assumed to satisfy Gaussian statistics, as in Sec. V, with independent random fluctuations from one coherence time to the next.

The plasma response to the laser field is found by solving linearized fluid equations that include the ponderomotive force term. Combining the continuity and momentum equations for the fluid plasma, linearizing in the flow velocity, and ignoring the second-order term $\nabla \ln(n_e)\nabla c_s^2$ one obtains a driven ion-acoustic wave equation for the quantity $L(x,z,t) \equiv \ln(n_e)$:

$$\left[\frac{\partial^2}{\partial t^2} + v_{ia}\frac{\partial}{\partial t} - c_s^2\nabla^2\right]L = \nabla^2 c_s^2 + \alpha\nabla^2|\Psi|^2 \tag{6.6}$$

21

where $\alpha = Ze^2/4m_e m_i \omega_0^2$, $c_s^2 = (ZT_e + T_i)/m_i$, and ν_{ia} is a heuristic damping rate. Linearization is justified by the fact that the fractional density and electron temperature perturbations were found to be typically $< 10\%$, especially in the ISI runs where rapid fluctuations of the interference structure tended to suppress large perturbations. In any case, most of the non-ISI simulations were carried out using a steady-state treatment, which does not require linearization. [The use of the variable $\ln(n_e)$ instead of n_e, preserves the correct ponderomotive nonlinear steady state behavior.] The ion temperature is assumed to be constant; ion-electron energy equilibration times are typically on the order of nanoseconds in these plasmas.

The ion-acoustic propagation and heat flow are expected to occur primarily in the transverse (x) direction. This stems from the following two considerations: (i) under the paraxial wave conditions assumed here the intensity variations occur primarily along x, and (ii) because the optical propagation speed $(\sim c)$ is so much larger than c_s, the ion-acoustic "wake" will propagate nearly normal to the optical axis z. Assuming then that all density disturbances propagate only along x, with relatively small variations in the sound speed, one can Fourier-transform Eq. (6.6) to yield:

$$\left[\frac{\partial^2}{\partial t'^2} + qk' \frac{\partial}{\partial t'} + k'^2 \right] \tilde{L}(k',z,t') = - \frac{k'^2}{c_{s0}^2} \left(\alpha |\Psi|^2 + c_s^2 \right) \tag{6.7}$$

where $t' \equiv tc_s/\lambda$, $k' \equiv k_x\lambda$ and $q \equiv \nu_{ia}/k_x c_s$ is the ratio of the imaginary/real frequency of the ion-acoustic wave. (In this paper q is taken to be $1/2$). The first term on the RHS of (6.7) is due to the ponderomotive force, and the second term is the plasma pressure due to thermal gradients. These source terms are assumed to be approximately constant over the time step used in the code (typically a picosecond or so). The solution to (6.7) for a source constant from t_0' to $t_0' + t_1'$ is:

$$L(k',t_0'+t_1') = \exp(-qk't_1'/2) \left\{ 1/\kappa[\partial L(k',t_0')/\partial t_0' + \frac{1}{2} qk'L(k',t_0') + \frac{1}{2}qk'G] \sin(\kappa t_1') \right.$$

$$\left. + \left[L(k',t_0') + G \right] \cos(\kappa t_1') \right\} - G \tag{6.8}$$

where $\kappa \equiv (1-q^2/4)^{1/2}k'$ and $G \equiv [\alpha |\Psi(k',t_0'+t_1'/2)|^2 + c_s^2(k',t_0'+t_1'/2)]/c_{s0}^2$. This result is inverse Fourier-transformed to yield the plasma density $n_e(x,z,t_0'+t_1')$ at the next time step.

The electron temperature is found by solving the relevant energy balance equation,

$$\frac{3}{2} n_e \frac{\partial}{\partial t} T_e = - \frac{\partial Q_e}{\partial x} + H . \tag{6.9}$$

where Q_e is the electron thermal heat flux, H is the joule heating source given by $H = \kappa_b |\Psi|^2$, and $\kappa_b(n_e,T_e)$ is the inverse bremmstrahlung absorption coefficient. Compression effects and electron-ion energy coupling are much smaller than the terms included in (6.9), and are ignored. A conservative flux-limited formalism is used for the heat flux; i.e.,

$$Q_e = \left[1 + \frac{\kappa_e |\partial T_e/\partial x|}{f_e n_e T_e \nu_e} \right]^{-1} \kappa_e \frac{\partial T_e}{\partial x} . \tag{6.10}$$

where κ_e is the electron thermal conductivity of the plasma and f_e is the flux limiter, which is set to 0.1 here in order to ensure that Q_e does not exceed its classical limit. (For the simulations presented here, the temperature gradients are small enough that the heat flux remains well below the classical limit; thus the magnitude of f_e has little effect on the results.) Equation (6.9) is solved by a predictor-corrector method with periodic boundary conditions. This can cause problems, because the net energy deposited by inverse bremmstrahlung cannot be lost to the plasma by either transverse heat flow losses or conversion to axial plasma kinetic energy. Therefore, the average energy gain $\bar{H}(z,t) \equiv \int dx\, H(x,z,t)/X_{len}$ is subtracted from the source term of (6.9) in order to keep the mean temperature at a given axial distance constant.

22

For steady-state problems, the calculation of the plasma density is simplified. The momentum equation for constant sources Ψ^2 and T_e reduces to $\nabla(c_i^2 n_e) + n_e \alpha \nabla \Psi^2 = 0$, yielding the solution

$$n(x,z) = \frac{C'}{c_i^2(x,z)} \exp\left[-\alpha \int^z \frac{\partial |\Psi|^2/\partial x'}{c_i^2(x',z)} \, dx'\right] . \tag{6.11}$$

where C' is a constant. The temperature T_e is found by iterative solution of Eq. (6.9) with arbitrary time steps, performed until the solution converges upon itself. These separate solutions for $T_e(x,z)$ and $n_e(x,z)$ are iterated alternately to obtain a convergent steady-state solution.

B. Results

The results presented here compare the filamentation behavior exhibited by ISI irradiation, conventional (quasi near field) focusing,[3] and the RPS technique.[22,23] For comparison purposes, we start with a simple well-defined laser-plasma model. First, the plasma is chosen to be homogeneous: the constant coupling parameters throughout the interaction region simplifies the analysis. Second, we ignore absorption in the plasma; absorption competes with filamentation, and can mask or eradicate the effect. While absorption is important in realistic conditions, it unnecessarily complicates the interpretation and comparison of the results. Both of these contraints are discarded later when we look at a "real plasma".

The plasma model is composed of a homogeneous 250 μm thick CH slab at $n_{eo} = 0.5n_c$ and $T_{eo} = 500$eV, irradiated by a .25 μm wavelength laser at 2×10^{14} W/cm^2. Under these conditions, perturbation theory[38] predicts that both the thermal and ponderomotive self-focusing lengths (for the fastest growing modes) are comparable (about 350λ). Thus, the interplay between these two mechanisms should be well represented here. Note that this plasma model is selected primarily to produce a very strong filamentation interaction; while useful for the purpose of comparison, it gives results that are more pessimistic than those of actual laboratory plasmas, as we will see later.

Three different cases are investigated: ISI irradiance, RPS irradiance, and the standard quasi near-field irradiance. Of these three, only the last is ambiguous in nature. We want the standard irradiance case to represent a typical high-power laser. In practice, the structure of quasi near-field illumination can vary greatly, depending upon the laser type, the power level, the optical engineering, the attention paid to beam quality, etc. Here, we select a 3:1 peak-to-average as characterizing the typical laser. The transverse mode spectrum of the incident plane waves is chosen to be flat for all spatial frequencies between π/R_{spot} and $N_S \Delta K = k/2$(F/number).

Two of these cases under scrutiny, the RPS and the standard laser case, require only the steady state analysis because the intensity patterns remain stationary in time. First consider the standard case, where the peak to average intensity value is 3:1 (the standard deviation is $\sigma_I = .51$). Figure 14 shows the intensity profile as a function of the propagation distance into the plasma. The first focal point appears at $z = 200\lambda$, and additional focal points appear with increasing frequency as the beam propagates farther into the plasma. This focal distance is shorter than the predictions using either the ponderomotive or thermal mechanisms alone; it is evidence that both mechanisms are acting together to promote filamentation. The filaments that are created appear to attract one another, and converge into a single large scale mode that has a high spatial frequency sub-structure. This behavior is caused by the interaction of the thermal and ponderomotive forces; the ponderomotive force is primarily responsible for the small initial filaments, since its fastest growing mode is approximately 40λ in width. Because thermal conduction spreads out temperature variations, the thermal filamentation mechanism only acts over larger distances. The fastest growing resolvable thermal mode is the same size as the simulation dimension, and this appears to be responsible for the large scale final mode. Note that the transverse spatial frequency structure of the irradiance changes fundamentally as the filaments are formed; after the first few filaments form, the structure is spread out over a much larger

23

region in frequency space. At first, these higher spatial frequency structures are locally coherent and form coherent filaments. Once these filaments interact with one another. however. the intensity pattern is randomized as the high frequency structure becomes incoherent on a much smaller scale. The resulting interference pattern seen in the final large scale mode then closely resembles the initial structure in the RPS method. Thus, once significant filamentation occurs and the modes interact (because of thermal self-focusing), further filamentation should be suppressed in accordance with RPS theory.[22]

In the RPS calculations, there is a moderate amount of suppression of filamentation if one uses small F-number ($<F$ 10) optics. Fig. 15 illustrates the reduction of filamentation that occurs as the F number decreases. As a measure of the degree of filamentation, the largest intensity occurring in the plasma is used. [Typical maximum/average values of the intensity profile *incident* on the plasma are as follows: (i) for the standard case $(I_{max}/I_{av})_{z=0} = 3$, (ii) for RPS $(I_{max}/I_{av})_{z=0} = 4$ to 6, (iii) for ISI $I_{max}/I_{av\ z=0} = 4$ to 5 and $(I_{max}/I_{av})_{z=0} = 1$.] For F number $>F$ 10, the maximum intensities are, on average, about 25% or more larger than for F number $<F$ 10. There may be better suppression below f/2.5, but the parabolic wave approximation begins to break down there, and the simulation results are not trustworthy. Also, the trend may be more pronounced at higher F number than shown here. The runs with larger F number do not include the longer wavelength modes, which are lumped into the DC term, and thus the peak initial intensities are somewhat lower than might otherwise be expected.

The ISI simulation was run for 350 coherence times $(t_c = 97$ psec), and most of the results presented here were averaged over this entire interval. The most important result is the time averaged intensity distribution shown in Fig. 16. This distribution exhibits the same development of high spatial frequency structure found in the standard laser case, but without the development of the attendant intensity peaks. The suppression of these peaks appears to be primarily due to the fact that the ISI irradiance structure constantly shifts around, not allowing any single filamentary structure to persist in the same spot.

However, the suppression is not complete on the shorter time scales. A typical instantaneous intensity distribution (Fig. 17) shows that filamentary structures are still present, although at a more modest level than in the standard case. To compare, Fig. 18 plots the values of I_{max}/I_{av} vs propagation distance for the standard case, along with the maximum value of the time-averaged ISI intensity (I_{max}), and the time average of the maximum ISI intensity (I_{max}). The ISI case is similar to the control case, except for two significant differences. First, the buildup of the intensity maximum takes much longer with ISI (with the first intensity maximum occurring around $z = 500\lambda$, as opposed to $z = 200\lambda$ in the standard case), meaning that ISI has lengthened the self-focusing distance. Second, the peak intensity with ISI is a factor of two lower than that found without ISI. This may be due to the smoothing effect in the time average, or it may be due to the smaller density channels made in the ISI process. (Note that although the averaged peak intensity in ISI is smaller than the standard case, the initial averaged peak intensity is larger.)

While ISI effectively suppresses filamentation of the time-averaged intensity, the behavior of the instantaneous intensity distribution in the plasma is still cause for concern, as many plasma instabilities have very short growth times ($\sim$ ps), and can therefore react to the peaks seen here. Fortunately, laser fusion pellets will not have densities $\sim 0.5\ n_c$ or sub-kilovolt temperatures extending over hundreds of laser wavelengths. As an example of a more realistic plasma, we present a simulation taken from a short-wavelength pellet interaction used in an earlier study.[9] The target is a DT pellet driven by a multi-megajoule laser, 26 nsec into the pulse, after a significant portion of plasma volume has been created. The temperature and density profiles used for this example are plotted in Fig. 19. To a good approximation the radial convergence can be ignored, and the target treated as planar. The major differences between this and the previous model are the inclusion of absorption (approximately 50% of the light is absorbed before $n = 5n_c$), higher temperatures, and the large

24

volume of plasma that is very underdense (and therefore more weakly coupled to the light). The results, as plotted in Fig. 20, show that ISI suppresses filamentation even on the short time scales, and negates filamentation as a problem. On the other hand, the results with the standard irradiation condition (2.25:1 peak to average) indicate that filamentation will be a nuisance without ISI (Fig. 21); here, a filament with a maximum intensity 9 times the incident average intensity has been formed.

VII. SUMMARY AND DISCUSSION

This paper has described the ISI technique in detail, and explored its potential application to direct-drive laser fusion. We have derived the ideal ISI profiles in the complete overlap and quadrature configurations [Eqs. (2.17) and (2.23), respectively], and examined the perturbing factors, such as multibeam interference, laser aberration, and plasma filamentation, which can introduce nonuniformities or limit the controllability of those profiles.

Using both analytic theory and numerical simulations, we have shown that ablation pressure nonuniformities due to the rapidly fluctuating interference structure are smoothed by two independent mechanisms. Thermal diffusion suppresses the higher spatial frequency components, in accordance with the "cloudy day" model. [E.g. see Eqs. (3.7) or (3.21a,b).] If this mechanism acted alone (as it would in the case of narrow bandwidth light) the standard deviation $\bar{\sigma}_n$ would be approximately proportional to $(\lambda/d)(f\,D)$ [Expression (3.25b)], which favors a large conduction zone width d and small overall F number $f\,D$. Temporal averaging provides an additional smoothing factor $\sigma_t \sim (t_c/\tau)^{1/2}$ [Eq. (3.19)], which favors a wide laser bandwidth $\Delta\nu = 1/t_c$ and a long pulse. The standard deviation $\sigma_n = \bar{\sigma}_n\sigma_t$ resulting from the combination of these two mechanisms is given approximately by expressions (3.25a,b); this result shows that ablation pressure nonuniformities ~ 1% should be attainable under laser-plasma conditions of interest to ICF. In the partial ISI scheme, there is a stationary component in the interference structure due to the coherent repeating steps. Although this component cannot be smoothed by temporal averaging, its spatial frequencies are sufficiently high that they are almost completely eliminated from the ablation pressure by the thermal smoothing mechanism. Thus, partial ISI may be one way to avoid the excessive pulse lengthening effects that would otherwise occur in large aperture systems where the number N_f^2 of independent beamlets could exceed $t_{pulse}/\Delta t$. If necessary, one could avoid the coherence between repeating steps by segmenting or multiplexing the laser beam itself, driving each segment by either separate oscillators or a different switched-out portion of a long single oscillator pulse.

The theory has shown that with ISI the average intensity profile at the target remains relatively insensitive to laser beam aberrations whose scale lengths s_{ab} are larger than the initial beamlet width D. In practice, this means that an incident beam aberrated to N_{ab} times its diffraction limit would require $N_f \geq 3N_{ab}$ echelon steps to ensure adequate control over the target profile. The aberration will tend to misalign and broaden this profile somewhat [Eqs. (4.10) or (4.12)], but it will not introduce any small-scale structure. In the usual case where $N_{ab} >> 1$ and the aberration arises primarily from random phase structure on the beam, the relative intensity perturbations due to misalignment and broadening are $R_1 \sim 1/N_f$ [Eq. (4.18)] and $R_2 \sim N_{ab}/N_f^2$ [Eq. (4.20)], respectively. Most of the broadening effect is controllable because it depends only upon spatial averages of the phase structure over the entire laser aperture; the uncontrollable component is $\Delta R_2 \sim N_{ab}/N_f^2$ [Eq. (4.22)]. Laser intensity nonuniformities can also contribute to perturbations of the ISI profile, especially in the quadrature configuration; however this effect also depends upon a spatial average over the aperture, and is expected to be negligible if $N_f >> 1$. Our results show that it should be possible to control the ISI intensity perturbations to within ~ 1%, even with the degree of aberration expected in realistic fusion drivers.

Two dimensional simulations of optical propagation using the SELFOCT code have shown that ISI significantly reduces filamentation in the underdense plasma, even in a non-absorbing, high density (0.5 n_c), low temperature (500 eV) slab, where a normal laser beam would experience intense filamentation. For low F number optics, the filamentation also appears to be inhibited by the

25

random-phase shift technique,[22-23] but to a lesser degree than with ISI. In simulations at 0.25 μm, including inverse bremsstrahlung, higher temperatures, and a more realistic plasma profile, the filamentation is virtually eliminated with ISI. (Fig. 20)

An important concern for ISI is the question of how broad bandwidths or transient nonuniformities would affect certain laser-plasma instabilities (e.g. parametric instabilities), which can respond much faster than the hydrodynamics. Earlier experiments at 1.054 μm indicated that although broad laser bandwidth suppressed stimulated Brillouin scattering in the underdense plasma, as predicted theoretically, the bandwidth appeared to enhance a critical region instability that produces fast electrons.[39-40] In the NRL experiments at 1 micron,[40] this effect was observed both with and without the ISI echelons. The bandwidths used in these experiments were comparable to the expected ion-acoustic frequency for the parametric decay instability, and the associated temporal mode beating may have been seeding this critical region instability. More recently,[20] the experiments were repeated at 0.527 μm to determine whether the use of a shorter laser wavelength, which is strongly absorbed before it reaches the critical region, would inhibit the fast electron generation. This indeed occurred; in fact, the experiments showed that with the combination of ISI and shorter wavelength, the enhanced hot electron generation observed earlier was replaced by a virtual quenching of hot electron production. In summary, the NRL experiments are consistent with the following model: (1) The smooth irradiance profile obtained with ISI echelons and broad bandwidth suppresses the effects of hot spots, preventing for example the seeding of self focusing. (2) The combination of this smoothing with the stabilizing effect of the bandwidth itself suppresses underdense parametric instabilities. (3) The shorter laser wavelength prevents light from reaching the critical region, and thereby suppresses broadband enhancement of hot electrons.

In the ISI and other related schemes discussed so far, the beam is divided up by optical arrays placed at the output of the laser, where coating damage and optical complexity[18,36] may be possible issues. This restriction on the location of the ISI arrays stems from self focusing effects in glass lasers, and from the necessity of maintaining spatial coherence in any harmonic conversion crystals. Near-field nonuniformities associated with an array of beamlets would seed self focusing if one attempted to amplify those beamlets in a multistage glass laser.[41] In KrF lasers, this restriction is no longer necessary because the amplifying medium is gaseous, intensities are low (typically < 10 MW/cm^2), and harmonic conversion is not required. The spatial incoherence could then be induced by echelons[42] or some alternative technique at a low energy stage within the laser, and optically-relayed through the remaining stages of the amplifier chain. For example, one could use reflection from a so-called plasma "spatial filter" to generate the spatially-incoherent light.[43] Although this technique is capable of producing a smooth focal spot,[43,44] it is not clear whether there would be sufficient control over the spatial coherence properties, or sufficiently rapid temporal averaging of the interference structure to ensure that the target profile is controllable. Alternatively, one could use the scheme shown in Fig. 22, in which a beam of statistically-homogeneous incoherent light is generated by broadband amplified spontaneous emission (ASE) in a mirrorless or spatially multimode oscillator.[21] This beam traverses a variable-density absorber, whose spatial transmission function $F(x)$ is the desired target beam profile. It is then focused onto the entrance pupil of an optically-relayed KrF laser chain. Because the entrance pupil lies at the Fourier transform plane of the absorber, the optical information needed to reproduce $F(x)$ at the target will be transported through the laser by a multitude of small coherence zones, rather than any large whole beam structure; thus the coherence zones play essentially the same role as the beamlets do in the conventional ISI. The target beam profile will be insensitive to laser imperfections as long as the coherence zones remain small in comparison to the transverse scale lengths of the phase aberration or amplifier gain nonuniformities. It will be insensitive to amplifier saturation if the coherence time t_c remains short in comparison to the KrF relaxation time (> 1 ns). Theoretical analysis, along with a preliminary experimental test using a small KrF oscillator-amplifier setup, has demonstrated that this technique is indeed capable of producing a smooth, controllable focal profile, even under non-optimum conditions.[21] Additional results on a larger KrF system will be reported in later publications.

APPENDIX

This Appendix calculates the moments of the target profile that the laser would produce without the ISI echelons. The coherent (but aberrated) amplitude in this plane is given by the diffraction integral[30]

$$E_C(\mathbf{x}, z, t) = \frac{k}{2\pi(f - z)} \int d^2x' \, E_L(\mathbf{x}', t) \exp\left[i\frac{k}{2(f-z)} |\mathbf{x}' - \mathbf{x}|^2 - i\frac{k}{2f}|\mathbf{x}'|^2 \right] \quad (A1)$$

Substituting expression (2.1) for $E_L(\mathbf{x}', t)$, one obtains the intensity

$$I_C(\mathbf{x}, z) = (c/8\pi) |E_C(\mathbf{x}, z, t)|^2$$

$$= \frac{C_C k^2 |F|^2}{(2\pi)^2(f-z)^2} \int d^2x' \int d^2x'' \, A(\mathbf{x}')A^*(\mathbf{x}'') \exp\left\{ -\frac{ik}{f-z} \left[(\mathbf{x}' - \mathbf{x}'')\cdot\mathbf{x} - \frac{z}{2f}(|\mathbf{x}'|^2 - |\mathbf{x}''|^2) \right] \right\} \quad (A2)$$

where $C_C = b^2 c/8\pi$. From Eq. (2.5) and the definition $b^2 = 8\pi/cD_1^2$, one obtains

$$\int I_C(\mathbf{x}, z) \, d^2x = |F|^2 \int \frac{d^2x'}{D_1^2} |A(\mathbf{x}')| = |F|^2 \quad (A3)$$

The centroid of $I_C(\mathbf{x}, z)$ is defined by Eq. (4.7)

$$|x_C|_z = \int I_C(\mathbf{x}, z)\cdot\mathbf{x}\, d^2x / \int I_C(\mathbf{x}, z)\, d^2x$$

$$= \left[\frac{k}{2\pi(f-z)D_1} \right]^2 \int d^2x' \int d^2x'' \, A(\mathbf{x}')A^*(\mathbf{x}'') \exp\left[i\frac{kz}{2f(f-z)}(|\mathbf{x}'|^2 - |\mathbf{x}''|^2) \right] \quad (A4a)$$

$$\times \left[\frac{f-z}{-ik} \right] \nabla' \int \exp\left[-\frac{ik}{f-z}(\mathbf{x}' - \mathbf{x}'')\cdot\mathbf{x} \right] d^2x \quad (A4b)$$

Performing the integration over $\mathbf{x}$, which gives $\delta(\mathbf{x}' - \mathbf{x}'')$, then integrating by parts over $\mathbf{x}'$, one finally obtains

$$|x_C|_z = \int \frac{d^2x'}{D_1^2} |A(\mathbf{x}')|^2 \left[\frac{f-z}{k} \nabla' \Phi(\mathbf{x}') + \frac{z}{f}\mathbf{x}' \right] . \quad (A5)$$

which reduces to (4.6a) for $z << f$. The second spatial moment is defined by

$$|x_C x_C|_z = \int I_C(\mathbf{x}, z)\, \mathbf{x}\mathbf{x}\, d^2x / \int I_C(\mathbf{x}, z)\, d^2x \quad (A6a)$$

$$= \left[\frac{k}{2\pi(f-z)D_1} \right]^2 \int d^2x' \int d^2x'' \, A(\mathbf{x}')A^*(\mathbf{x}'') \exp\left[\frac{ikz}{2f(f-z)}(|\mathbf{x}'|^2 - |\mathbf{x}''|^2) \right]$$

$$\times \left[\frac{f-z}{k} \right]^2 \nabla' \nabla'' \int \exp\left[-\frac{ik}{f-z}(\mathbf{x}' - \mathbf{x}'')\cdot\mathbf{x} \right] d^2x \quad (A6b)$$

Following steps similar to those used on (A4), one obtains expression (4.6b) for $z << f$.

27

ACKNOWLEDGMENTS

REFERENCES

1. J. Nuckolls, L. Wood, A. Thiessen, and G. Zimmerman, Nature **239**, 139 (1972)

2. S.E. Bodner, J. Fusion Energy **1**, 221 (1981).

3. S.P. Obenschain, J. Grun, B.H. Ripin, and E.A. McLean, Phys. Rev. Lett. **46**, 1402 (1981); S.P. Obenschain, R.R. Whitlock, E.A. McLean, B.H. Ripin, R.H. Price, D.W. Phillion, E.M. Campbell, M.D. Rosen, and J.M. Auerbach, Phys. Rev. Lett. **50**, 44 (1983).

4. M.H. Emery, J.H. Orens, J.H. Gardner, and J.P. Boris, Phys. Rev. Lett. **48**, 253 (1982).

5. J.H. Gardner and S.E. Bodner, Phys. Rev. Lett. **47**, 1137 (1981).

6. J.E. Howard, Appl. Opt. **16**, 2764 (1977).

7. S. Skupsky and K. Lee, J. Appl. Phys. **54**, 3662 (1983).

8. L.M. Goldman, R.E. Hopkins, L.D. Lund, R.L. McCrory, S. Skupsky, and K. Walsh, *Fusion Engineering Program, Nuclear Engineering Department, University of Wisconsin UWFDM-568* (March 1984); S. Skupsky, R.L. McCrory, P. McKenty, and C. Verdon, *Fusion Technology Institute, University of Wisconsin UWFDM-651* (Sept. 1985).

9. A.J. Schmitt, Appl. Phys. Lett. **44**, 399 (1984).

10. J.M. McMahon, R.P. Burns, T.H. DeRieux, R.A. Hunsicker, and R.H. Lehmberg, IEEE J. Quantum Electron. QE-17, 1629 (1981).

11. *University of Rochester Laboratory for Laser Energetics Annual Report* (1 Oct. 1983-30 Sept. 1984) edited by R.L. McCrory; M.C. Richardson, et al., Digest of the 1985 Conference on Lasers and Electro-Optics (Baltimore, MD, 21-24 May, 1985).

12. "Optical Phase Conjugation," Edited by R.A. Fisher (Academic Press, New York, 1983).

13. J. Goldhar and J.R. Murray, IEEE J. Quantum Electron. QE-18, 399 (1982).

14. J. Goldhar, M.W. Taylor, and J.R. Murray, IEEE J. Quantum Electron. QE-20, 772 (1984)

15. R.S.F. Chang, R.H. Lehmberg, M.T. Duignan, and N. Djeu, IEEE J. Quantum Electron. QE-21, 477 (1985); J. Reintjes, R.H. Lehmberg, R.S.F Chang, M.T. Duignan, and G. Calame, J. Opt. Soc. Am. B3, 1408 (1986).

16. R.H. Lehmberg, Opt. Commun. **43**, 369 (1982), J. Opt. Soc. Am. **73**, 558 (1983)

17. R.H. Lehmberg and S.P. Obenschain, Opt. Commun. **46**, 27 (1983)

18. A.J. Schmitt, R.H. Lehmberg, J.A. Gardner, and S.E. Bodner, *Fusion Technology Institute, University of Wisconsin UWFDM-651* (Sept. 1985)

19. A.J. Schmitt and J.H. Gardner, J. Appl. Phys. **60**, 6 (1986).

20. S.P. Obenschain, J. Grun, M.J. Herbst, K.J. Kearney, C.K. Manka, E.A. McLean, A.N Mostovych, J.A. Stamper, R.R. Whitlock, S.E. Bodner, J.H. Gardner, and R.H. Lehmberg, Phys. Rev. Lett. **56**, 2807 (1986)

21. R.H. Lehmberg, S.P. Obenschain, M. Pronko, and J. Goldhar, Digest of the 1986 Conference on Lasers and Electro-Optics (San Francisco, CA, 9-13 June, 1986); R.H. Lehmberg and J Goldhar, Fusion Technol. (in press); *Naval Research Laboratory Memorandum Report 5829* (14 August, 1986).

22. K. Mima and Y. Kato, *Institute of Laser Engineering Progress Report on Inertial Fusion Program* (May 1982); Y. Kato and K. Mima, Appl Phys. **B29**, 186 (1982).

23. Y. Kato, K. Mima, N. Miyanaga, S. Arinaga, Y. Kitagawa, M. Nakatsuka, and C. Yamanaka, Phys. Rev. Lett. **53**, 1057 (1984).

24. C.B. Burckhardt, Appl. Opt. **9**, 695 (1970).

25. Y. Kawamura, Y. Itagaki, K. Toyoda, and S. Namba, Opt. Commun. **48**, 44 (1983).

26. Spawr Optical Research, Inc., Corona, CA; U.S. Patent No. 41, 959, 131 (1980).

27. D.M. Dagenais, J.A. Woodroffe, and I. Itzkan, Appl. Opt. **24**, 671 (1985).

28. Ximing Deng, Xiangchun Liang, Zezun Chen, Wenyan Yu, and Renyong Ma, Appl. Opt. **25**, 377 (1986).

29. M.A. Summers, G.J. Linford, and J.D. Williams, *1983 Laser Program Annual Report UCRL-50021-83* (Lawrence Livermore National Laboratory, Livermore, CA, 1984); R.A. Haas, M.A Summers, and G.J. Linford, Opt. Lett. **11**, 620 (1986).

30. M. Born and E. Wolf, "Principles of Optics" (New York: Pergamon Press, 1964) Chapt 8

31. T.W. Johnson and J.M. Dawson, Phys. Fluids **16**, 722 (1973).

32. Carl W Helstrom, "Statistical Theory of Signal Detection" second edition (Pergamon Press, New York, 1968) Sec. IId

33. S.N. Vlasov, V.A. Petrishchev, and V I. Talanov, Izv. VUZ Radiofiz **14**, 1353 (1971)

34. J.I. Davis, Appl. Opt. **5**, 139 (1966).

35. L.A. Rosocha, P S. Bowling, M.D Burrows, M Kang, J Hanlon, J McLeod, and G W York, Jr., Laser and Particle Beams **4**, 55 (1986).

36. R.H. Lehmberg, S P Obenschain, and A.J Schmitt, NRL Memorandum Report 5713 (31 Dec 1985).

37. J.A. Fleck, Jr., J R. Morris, and M D Feit, Appl Phys. **10**, 129 (1976), **14**, 99 (1977)

38. M J Herbst, J A Stamper, R H Lehmberg, R R Whitlock, F C Young, J Grun, and B H Ripin, *Nonuniformities in Laser-Ablated Plasma*, Naval Research Laboratory Memorandum Report 4983 (30 Dec 1982)

39. C. Yamanaka. T. Yamanaka. T. Sasaki. J. Mizui. and H.B. Kang. Phys. Rev. Lett. 32, 1038 (1974).

40. S.P. Obenschain. et al.. Digest of the Thirteenth International Quantum Electronics Conference. reprinted in J. Opt. Soc. Am. B **1**, 470 (1984)

41. D.C. Brown. "High-Peak-Power Nd: Glass Laser Systems" (New York: Springer-Verlag. 1981) Sec. 1.6.

42. H. Schönnagel. H. Gunkel. and J. Grzanna. Laser and Particle Beams **4**, 453 (1986).

43. V.V. Alekxandrov. M.V. Brenner. S.V. Loburev. N.G. Koval'skii and A.M. Rubenchik. Sov. J. Quantum Electron. **16**, 443 (1986).

44. D.E. Solomon and T.M. Henderson. J. Phys. D **8**, L85 (1975).

BEAM SMOOTHING BY
INDUCED SPATIAL INCOHERENCE (I.S.I.)

LASER BEAM OF
BANDWIDTH
$\Delta\nu = 1/t_c$

D_1

$t_{n+1} - t_n$

TRANSPARENT
ECHELON

f

$2f\lambda/D_1$

$t_c > t_N - t_1$

$t_c < t_{n+1} - t_n$

FOCAL IRRADIANCE
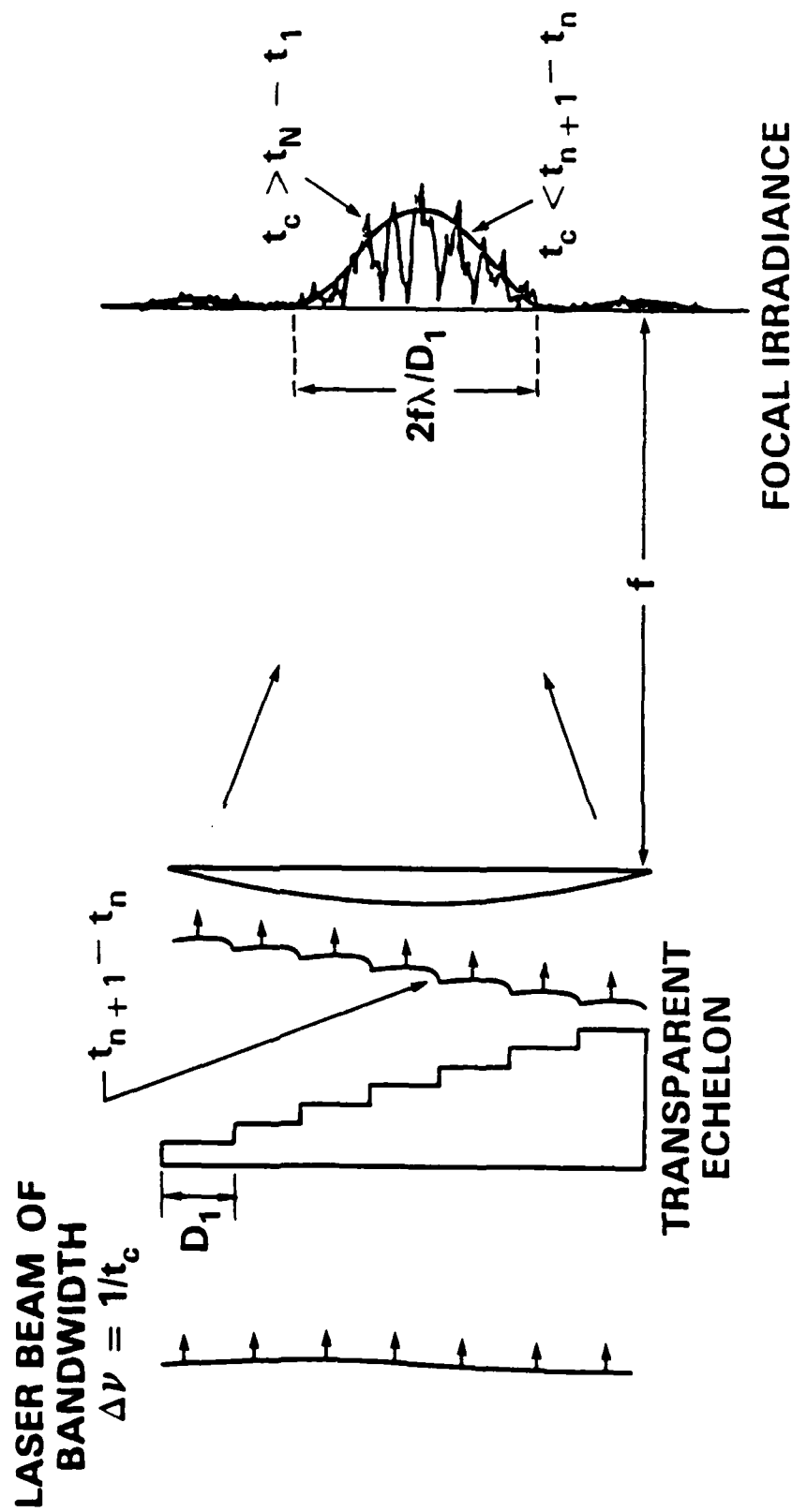
Figure 1 — Schematic of the ISI concept in two dimensions. The broadband laser beam of coherence time t_c is broken up into mutually incoherent beamlets if the echelon-induced time delay increments satisfy $t_{n+1} - t_n > t_c$. The lens combines these beamlets at its focal point to give a profile that has a smooth time average for times $> t_c$.

31
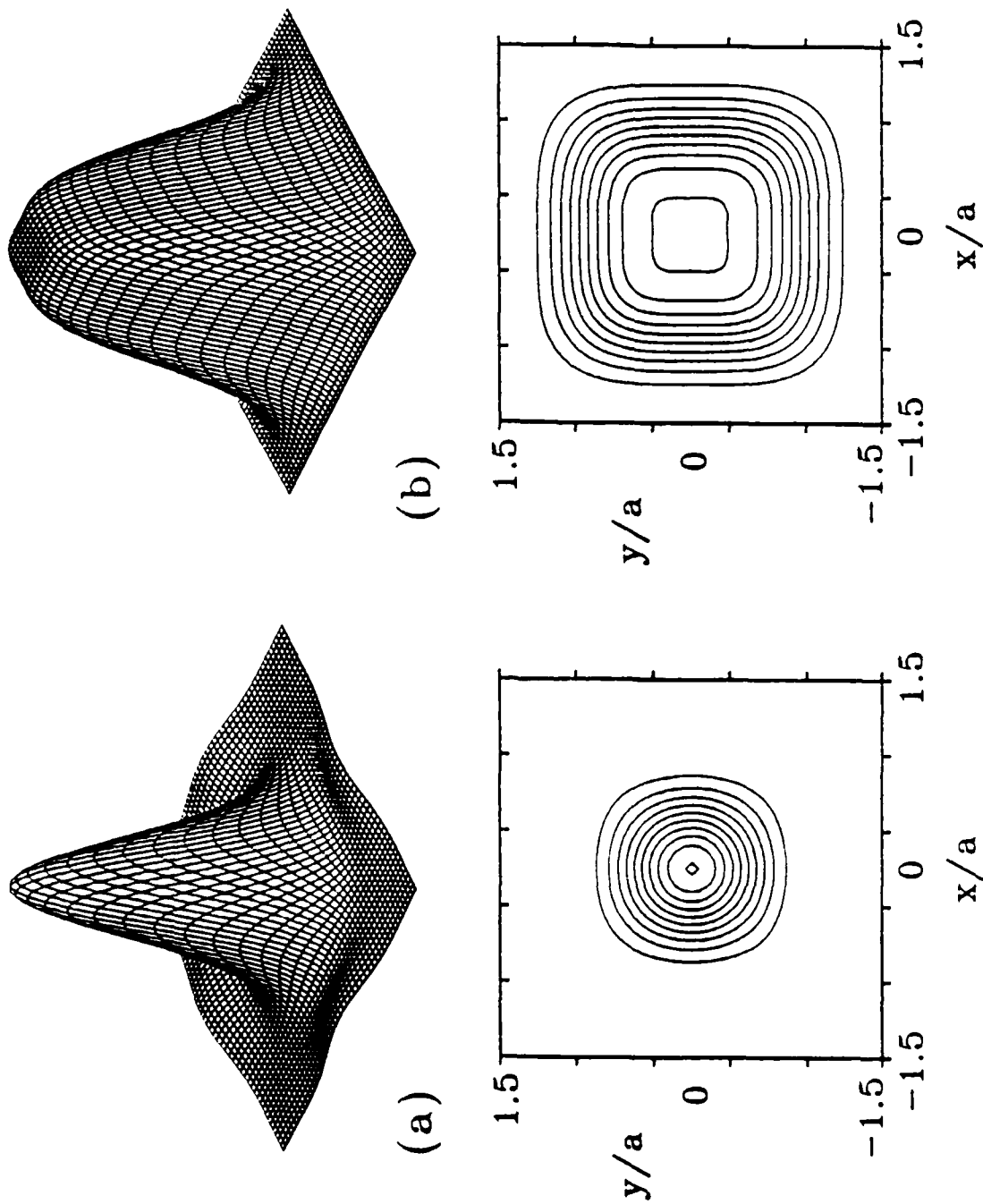
Figure 2 — Time-averaged beam profiles produced by the ISI technique with echelon steps that are (a) all parallel, and (b) alternately tilted in opposite directions to produce overlapped profiles whose centers are separated from one another by 43% of their individual spot sizes. In the bottom contour plots, the contours are shown at every 10% of peak fluence.

32

ALTERNATE TECHNIQUE FOR ACHIEVING I.S.I.
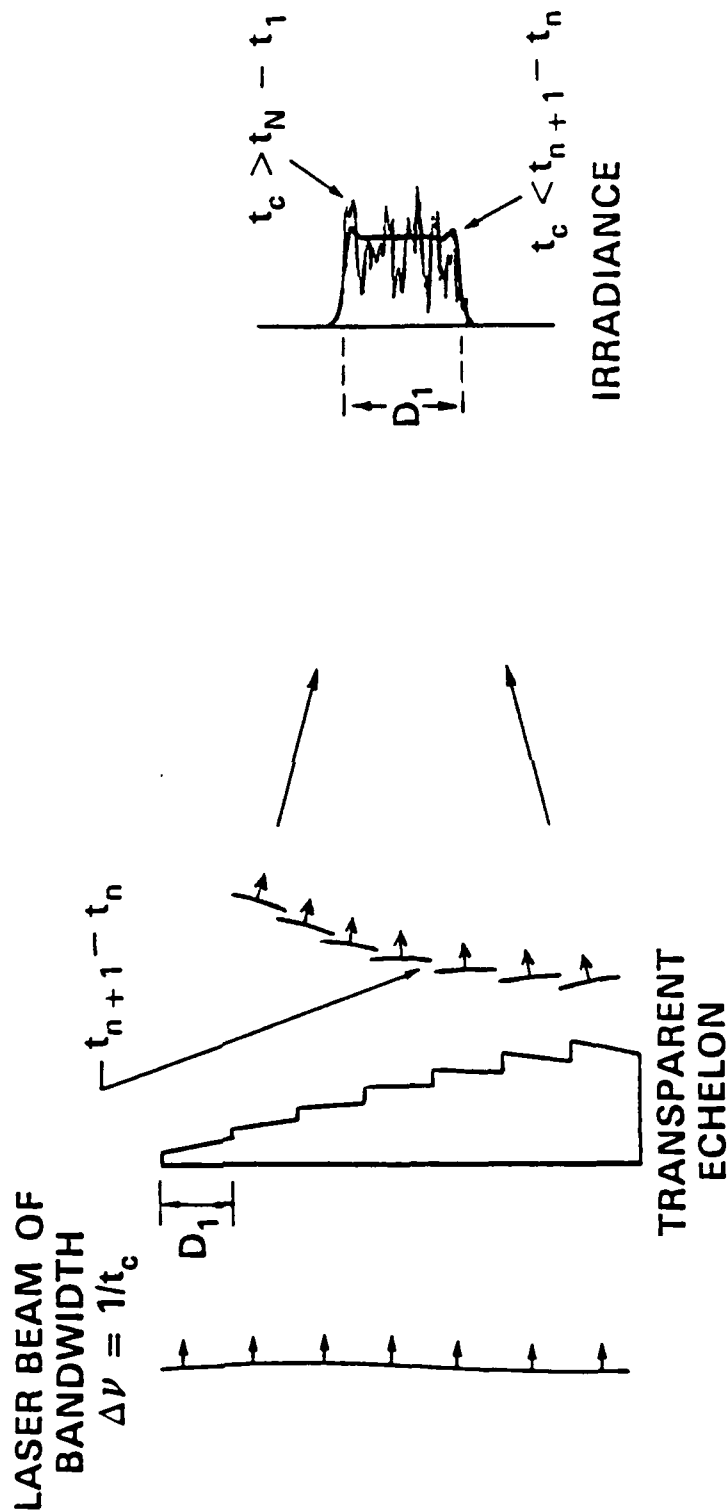
Figure 3 — alternative ISI configuration in which the steps are tilted so that the beamlets overlap in the quasi near-field. The resulting "flat-topped" profile will have nonuniformities due to Fresnel diffraction, unless each step is apodized.
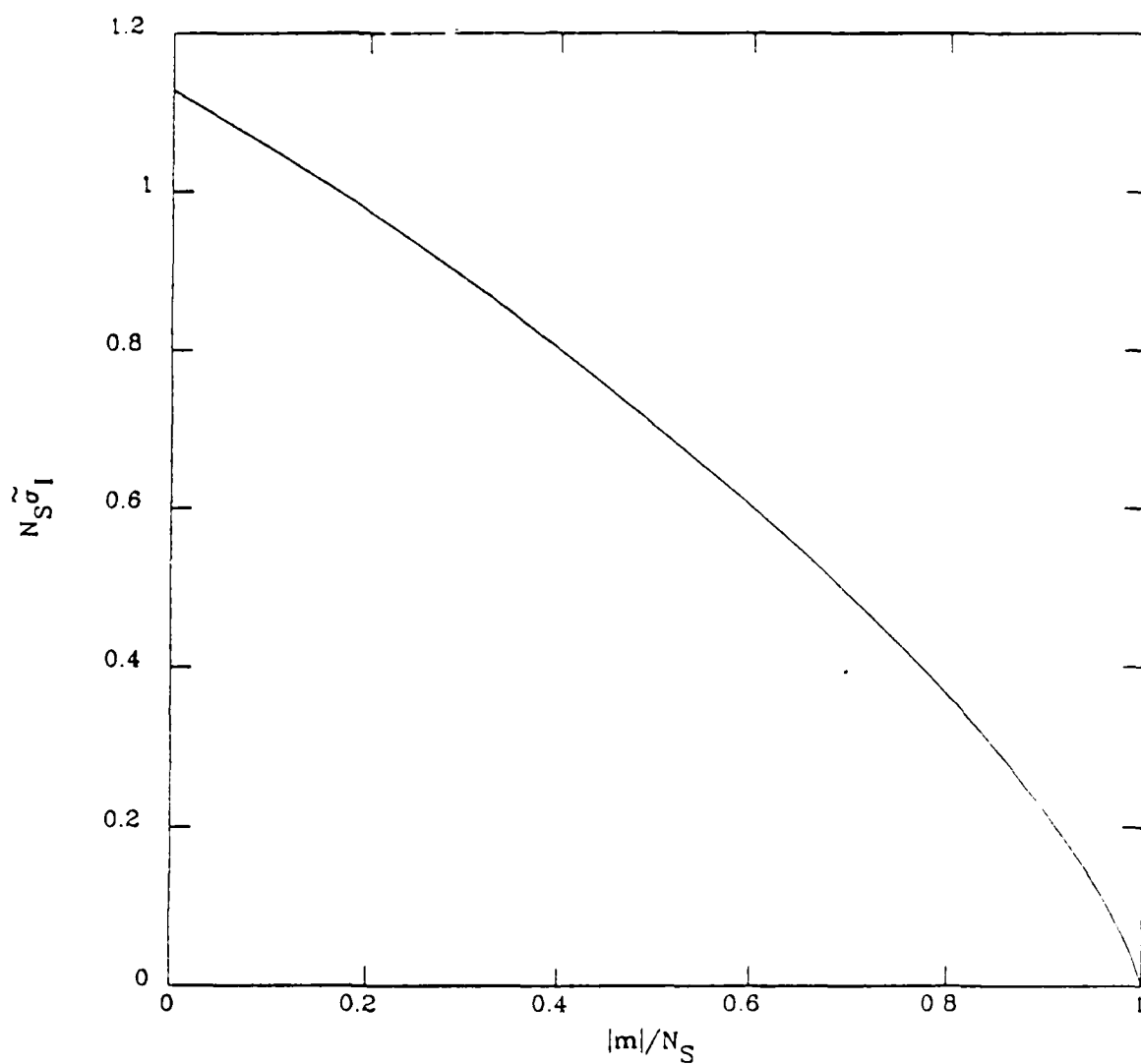
Figure 4 — Relative RMS mode amplitudes of the intensity nonuniformities [Eq. (3.22)] × (number of echelon steps N_S) vs. reduced mode number $|m|/N_S$, assuming no temporal averaging.
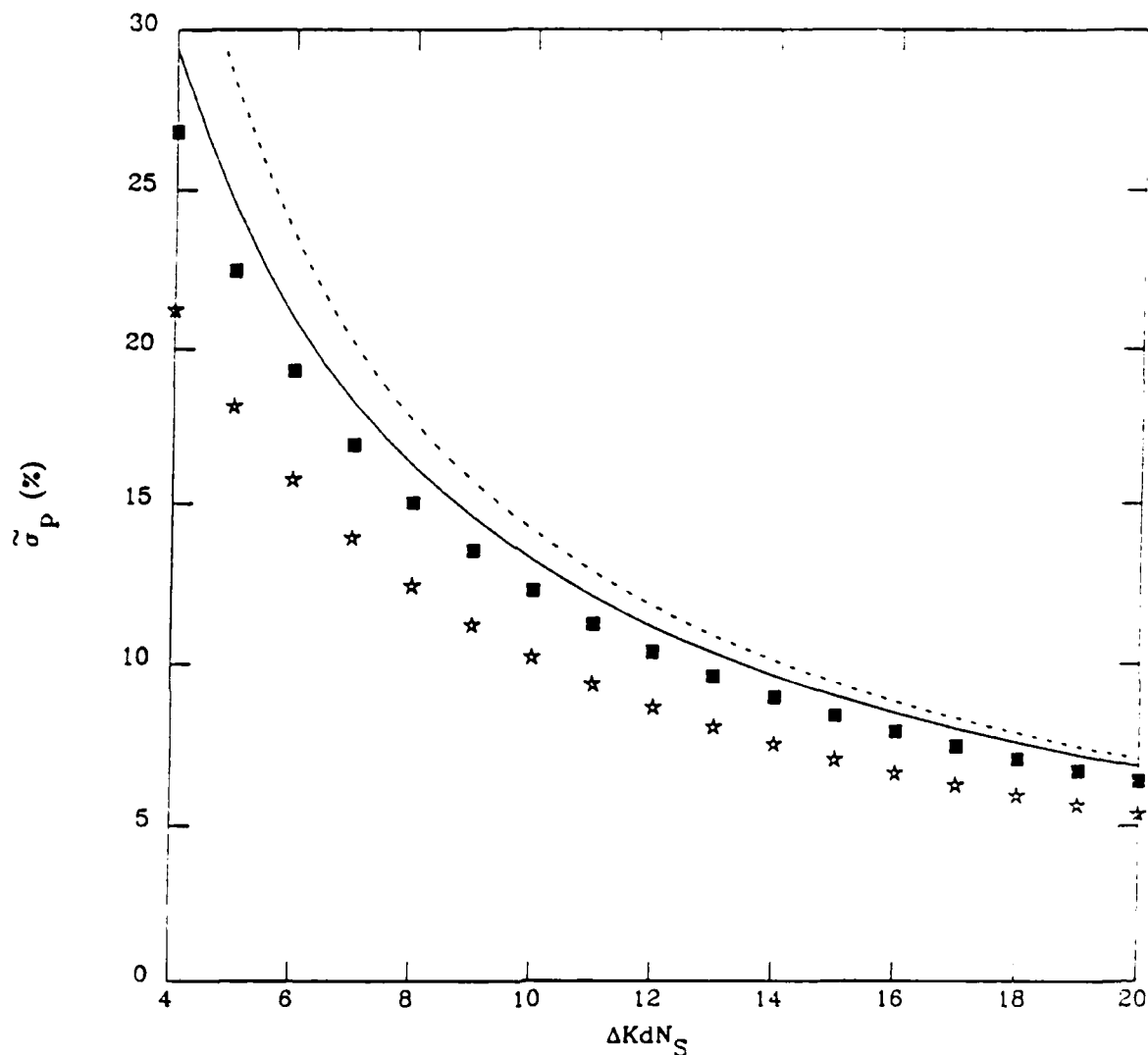
Figure 5 — Standard deviation of the ablation pressure nonuniformities [Eq. (3.24)] vs. dimensionless parameter $\Delta KdN_S = (2\pi d/a)N_S$ (assuming no temporal averaging) for values of the fixed parameter $\Delta Kd \ll 1$ (solid line), $\Delta Kd = 0.5$ (squares), and $\Delta Kd = 1.0$ (stars). The dashed line is the asymptotic result $\bar{\sigma}_p - 2^{1/2}/\Delta KdN_S$ [Expression (3.25b)], which becomes exact in the limit where $\Delta Kd \ll 1$ and $\Delta KdN_S \gg 1$.
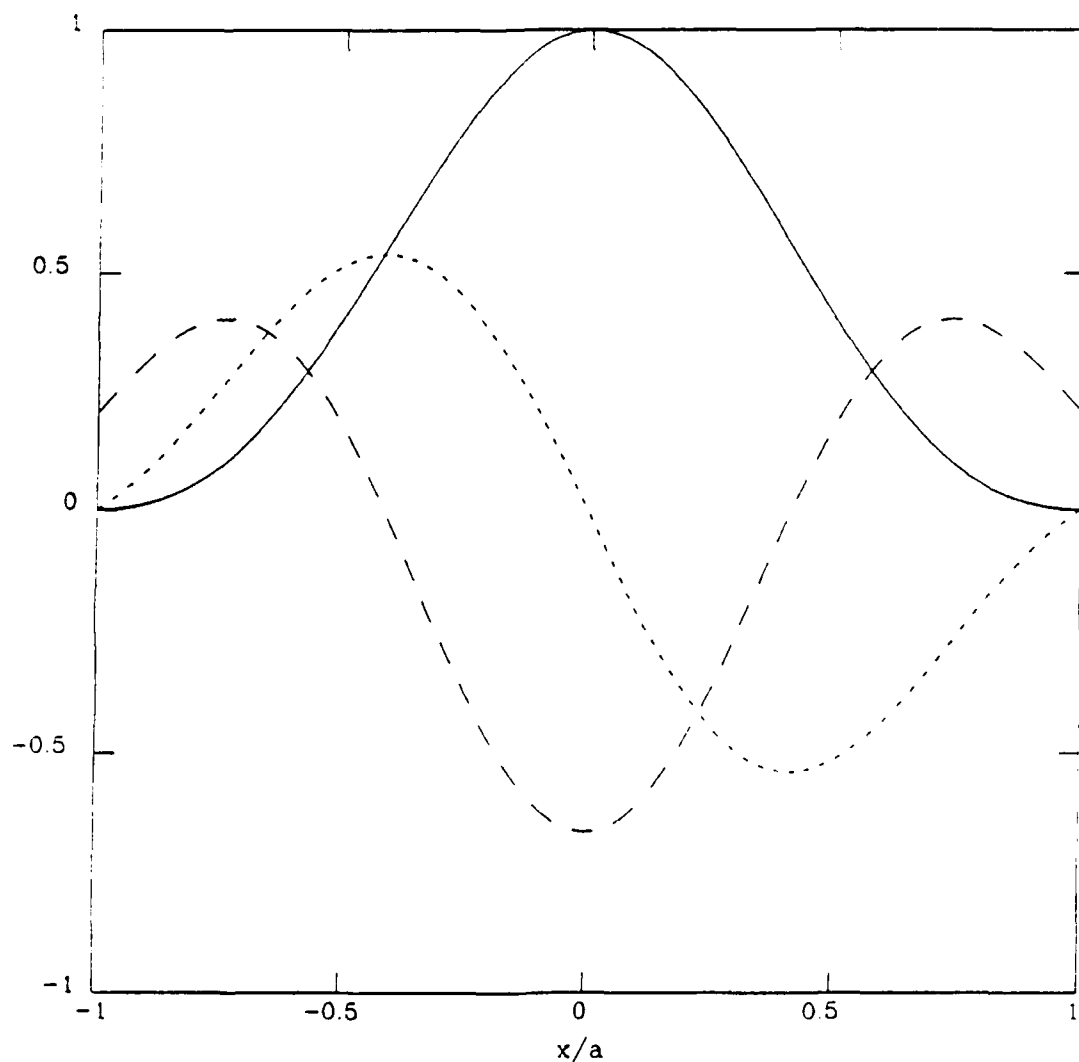
Figure 6 — Ideal sinc^2 profile $S(\pi x/a, 0)$ [defined by Eq. (2.17)] and its first and second derivatives [defined by Eqs. (4.11)], which are used to calculate perturbations of the time-averaged ISI profile due to laser beam aberration. The solid line shows $S(\pi x/a,0)$, dotted line shows $S'_x(\pi x/a,0)$, and dashed line shows $S''_{xx}(\pi x/a,0)$.
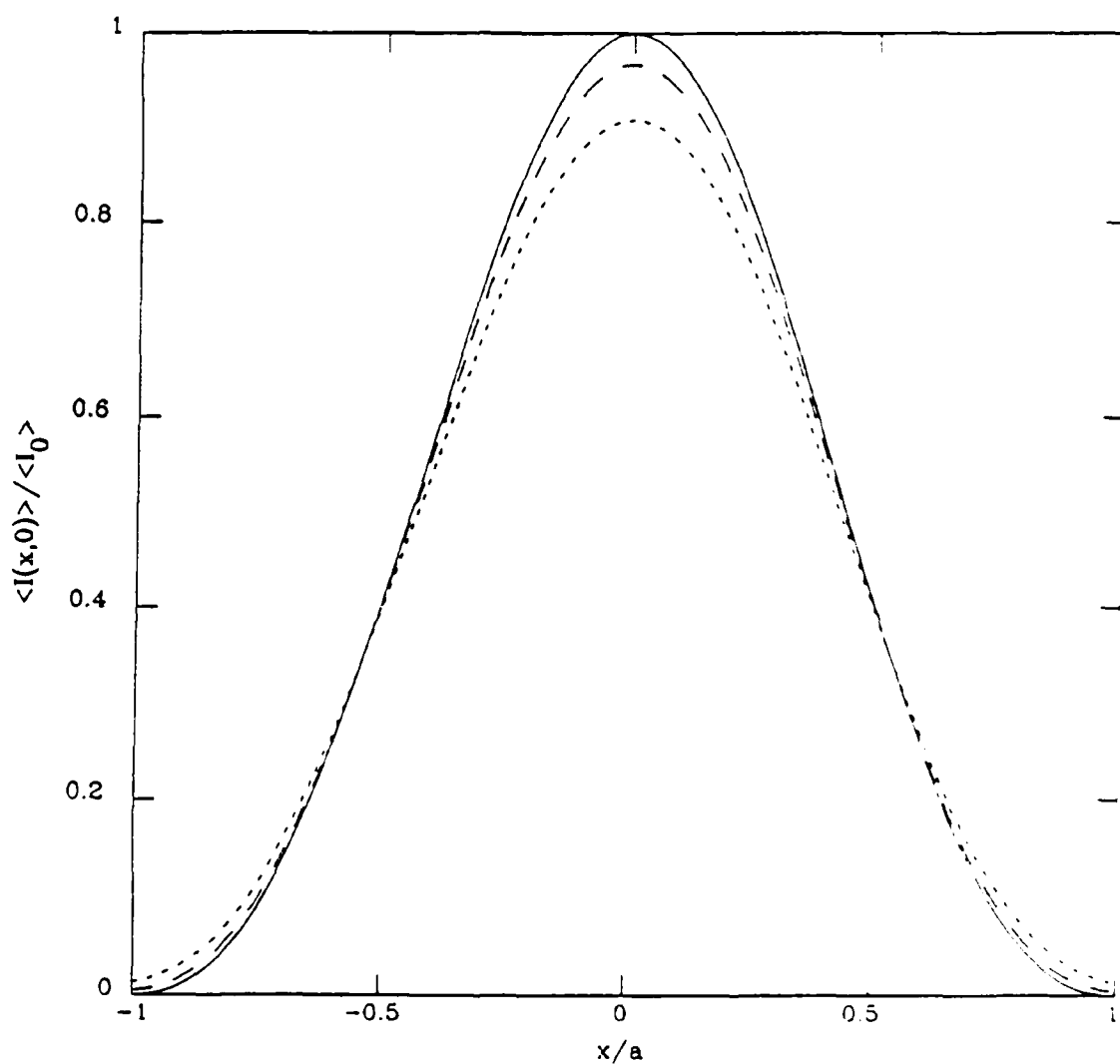
Figure 7 — Time-averaged ISI profiles calculated from expressions (4.10) and (4.11), assuming $|x_c| = 0$ and ISI broadening factor $a/2[|x_c|^2]^{1/2}$ equal to ∞ (solid line), 5 (dashed line), and 3 (dotted line).

37

QUASI NEAR FIELD FOCUSING OF AN ABERRATED LASER BEAM
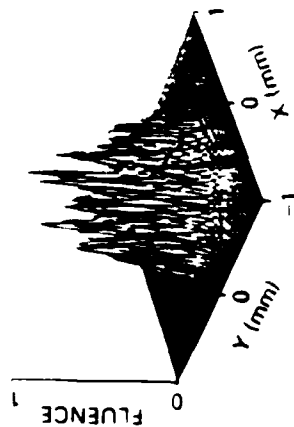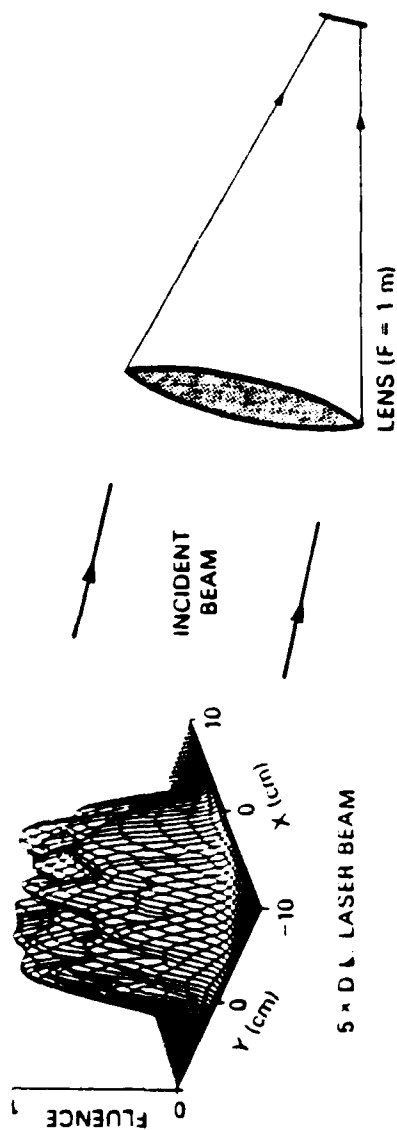
FLUENCE AT THE ABSORPTION REGION

ABLATION PRESSURE, ASSUMING
THERMAL SMOOTHING WITH d = 50 μm.

Figure 8   Numerical simulation of the conventional focusing geometry, where the target is placed in the quasi near field of the 5 × DL aberrated laser beam. The ablation pressure retains large nonuniformities in spite of the thermal smoothing.

RANDOM PHASE BEAMLETS WITH
NARROW BANDWIDTH LIGHT
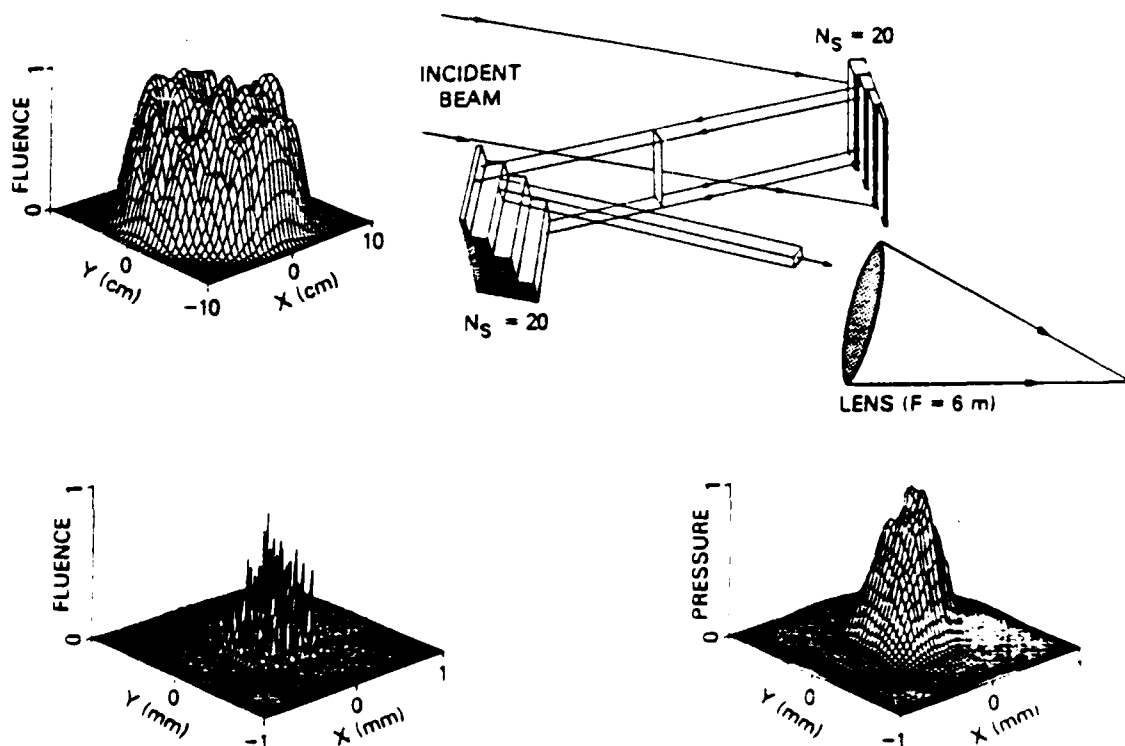
FOCAL POINT FLUENCE, ASSUMING
THAT THE ECHELONS ARE ILLUMINATED
BY A MONOCHROMATIC LASER.
INTERFERENCE PATTERN IS "FROZEN IN."

ABLATION PRESSURE, ASSUMING
THERMAL SMOOTHING WITH d = 50 μm.

Figure 9 — Numerical simulation of the quadrature configuration (using reflecting echelons with $N_S = 20$ and $D_1 = 1$ cm) illuminated by narrowband 527 nm light. The resulting stationary interference pattern is partially filtered out of the ablation pressure, but the lower spatial frequencies remain, giving a 37% peak/valley deviation from the ensemble-averaged profile $p(x)$.

I.S.I. WITH BROADBAND LIGHT

FOCAL POINT FLUENCE WITH THE
ECHELONS IN PLACE, AND A BROADBAND
LASER INTEGRATED OVER TIME INTERVAL
$\tau = 100\ t_c$.

ABLATION PRESSURE, ASSUMING
THERMAL SMOOTHING WITH $d = 50\ \mu m$.
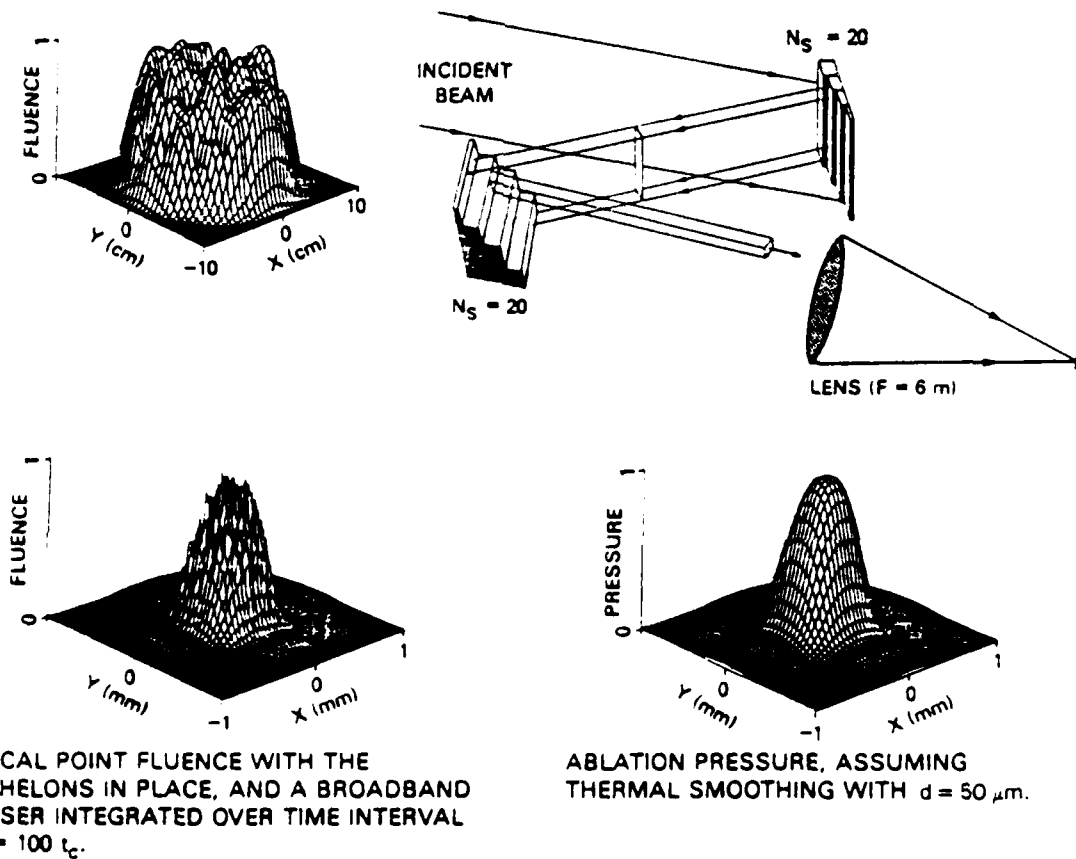
Figure 10 — Numerical simulation of ISI with broadband 527 nm light, showing the quadrature intensity and ablation pressure profiles averaged over 100 coherence times. The peak/valley deviation from the ensemble-averaged ablation pressure is now 2.4%.
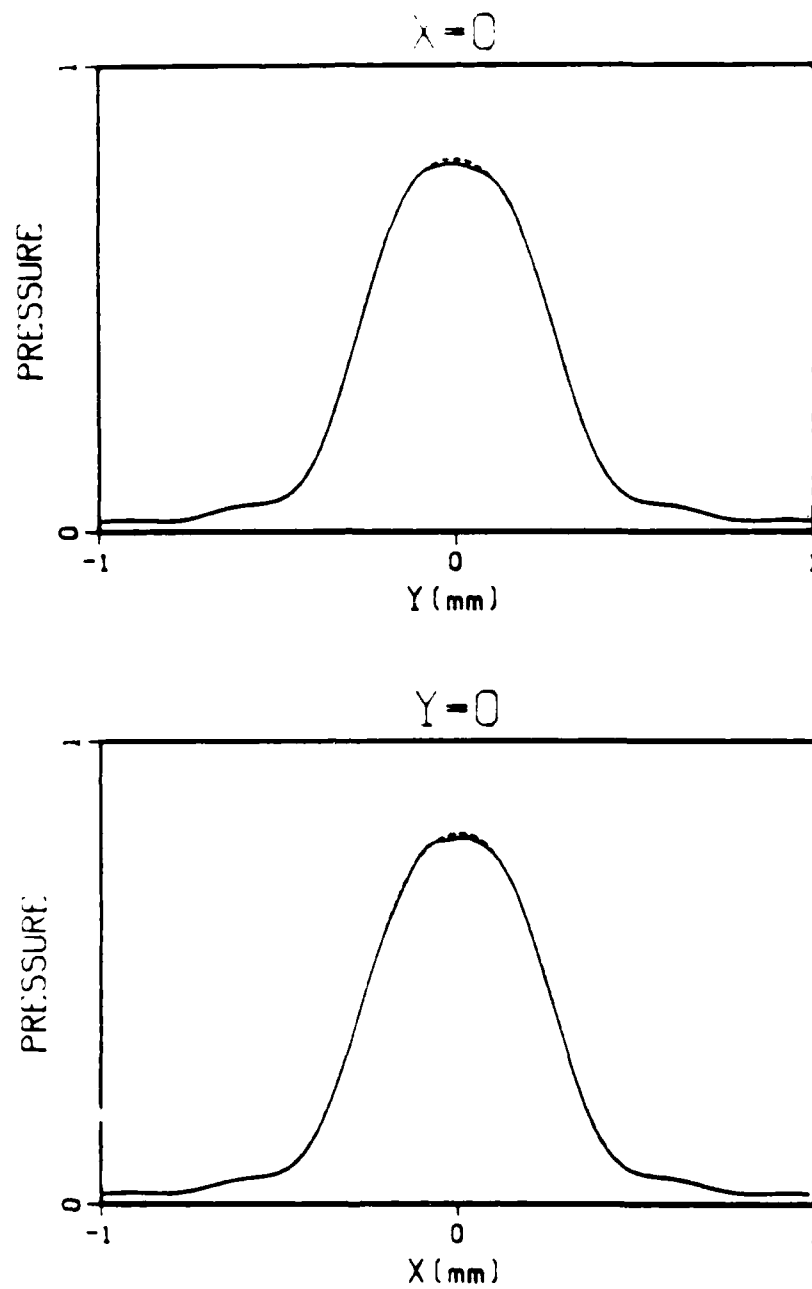
40
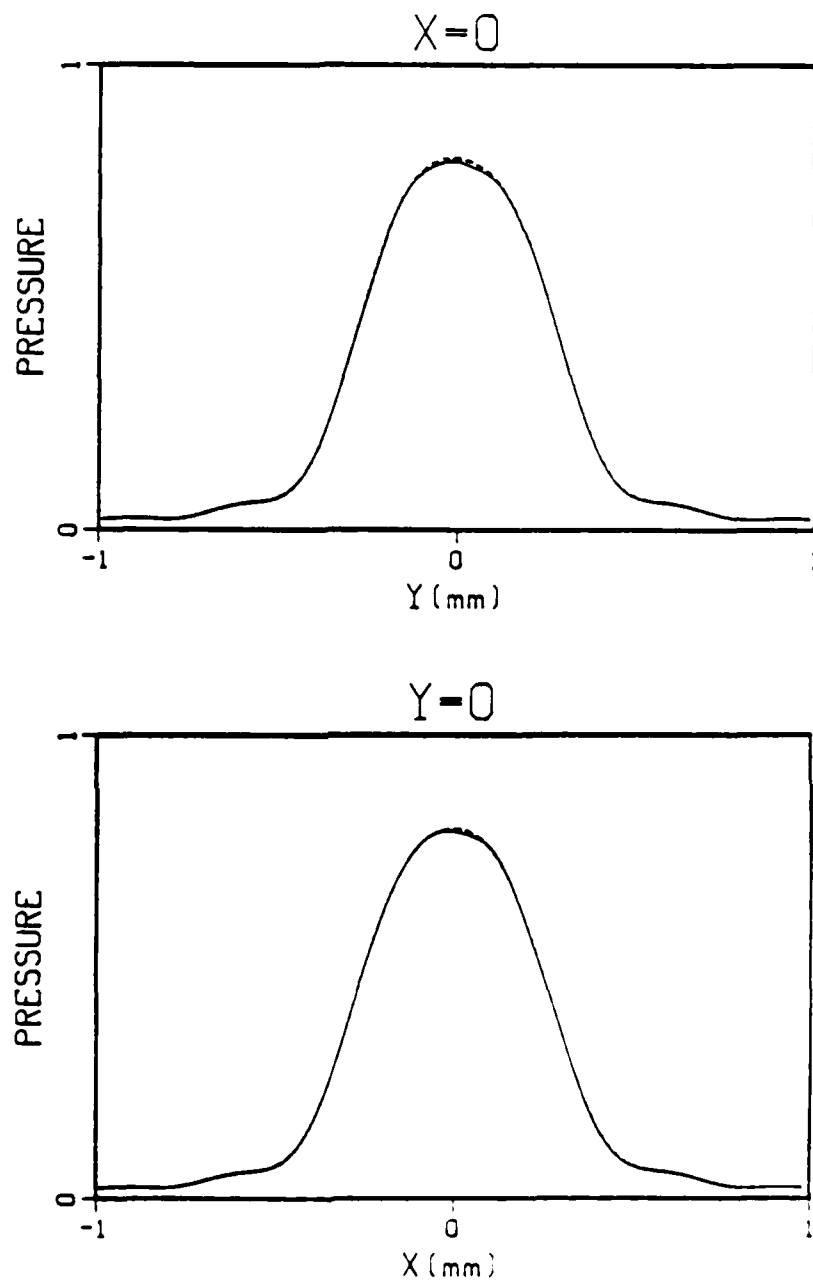
Figure 11 — Horizontal and vertical slices through the center of the ablation pressure profile shown in Fig. 10. The dashed lines show the ensemble-averaged profiles $p(x,0)$ and $p(0,y)$.
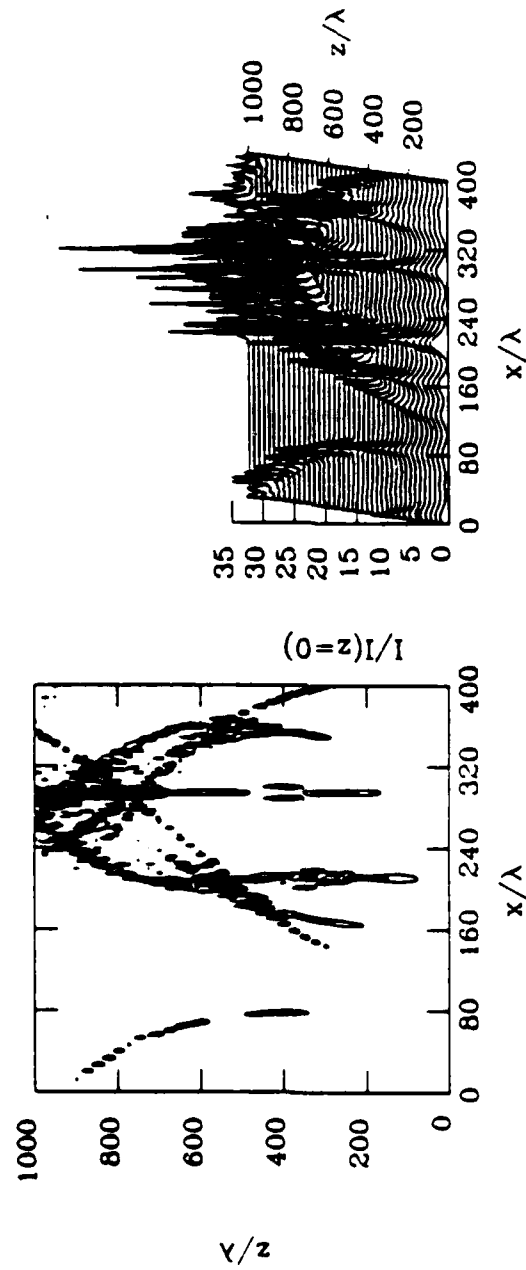
PARTIAL ISI SCHEME USING REPEATED STEPS

TWO REPEATED 10
STEP ECHELONS

LENS (F = 6 m)

TWO REPEATED 10
STEP ECHELONS

INCIDENT
BEAM
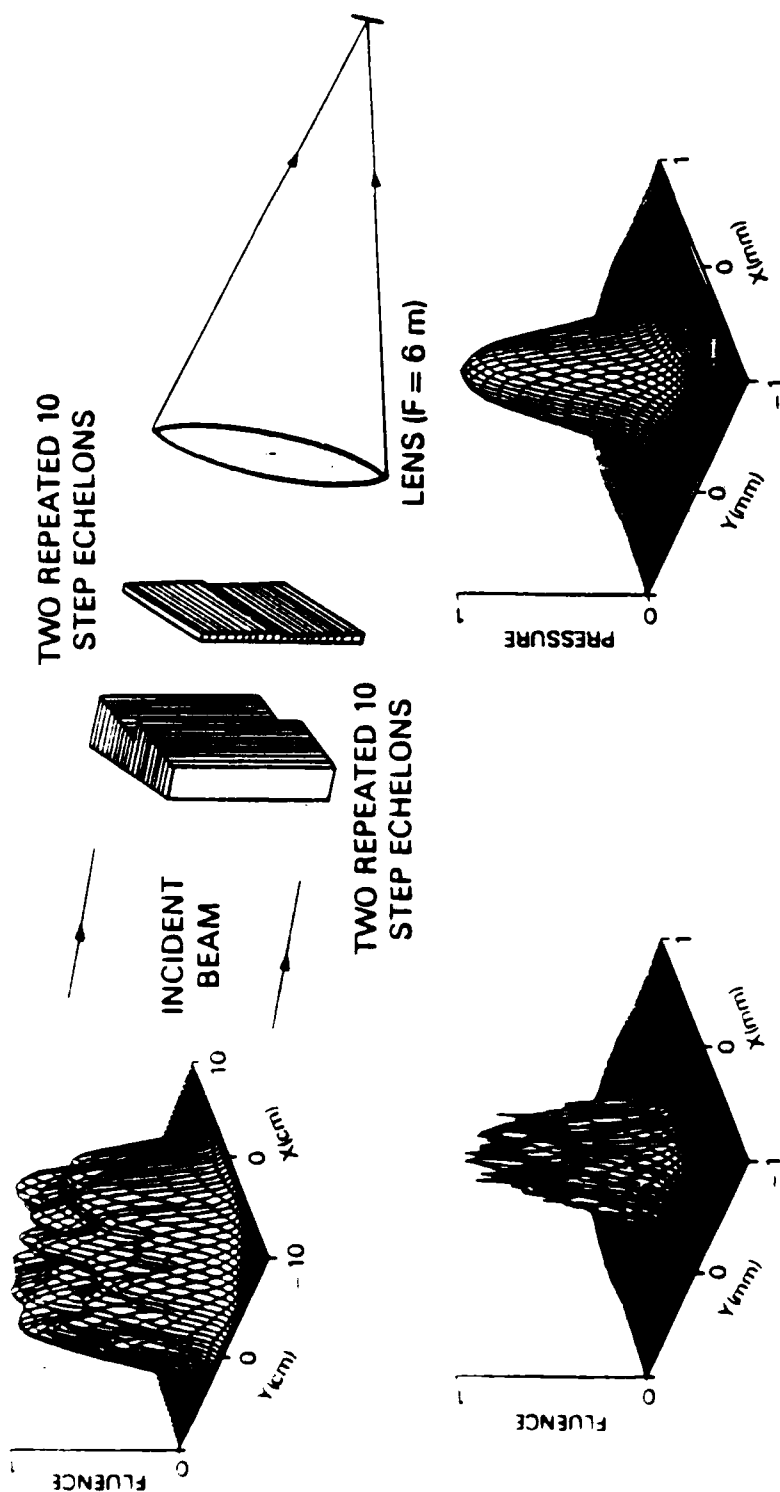
FLUENCE

FOCAL POINT FLUENCE WITH THE
REPEATED ECHELONS AND A
BROADBAND LASER INTEGRATED
OVER TIME INTERVAL $\tau = 100\ t_c$.

ABLATION PRESSURE, ASSUMING
THERMAL SMOOTHING WITH d = 50 μm.

PRESSURE

FLUENCE

Figure 12   Numerical simulation of the partial ISI concept with broadband 527 nm light   The time delay sequence repeats after 10 steps, thus giving the stationary high spatial frequency interference components in the fluence   Thermal smoothing removes these components from the ablation pressure, thus reducing the peak valley nonuniformities to 3.9%

42

Figure 13 — Horizontal and vertical slices through the center of the ablation pressure profile shown in Fig. 12. The dashed lines show the ensemble-averaged profiles $p(x,0)$ and $p(0,y)$

$I/I(z=0)$

35
30
25
20
15
10
5
0

0 80 160 240 320 400
x/λ

1000
800
600
400
200
z/λ

1000
800
600
400
200
0

0 80 160 240 320 400
x/λ

z/λ

Figure 14 — Contour and isometric plot of the intensity for a typical laser profile (3:1 peak-to-average intensity variations, $a_{rms} = 0.51$) incident on a slab of $5n_{crit}$ CH plasma at 500eV. Contours are at $2.2I_0$, which is 10% of the peak laser intensity. Laser propagates along the z axis.

44
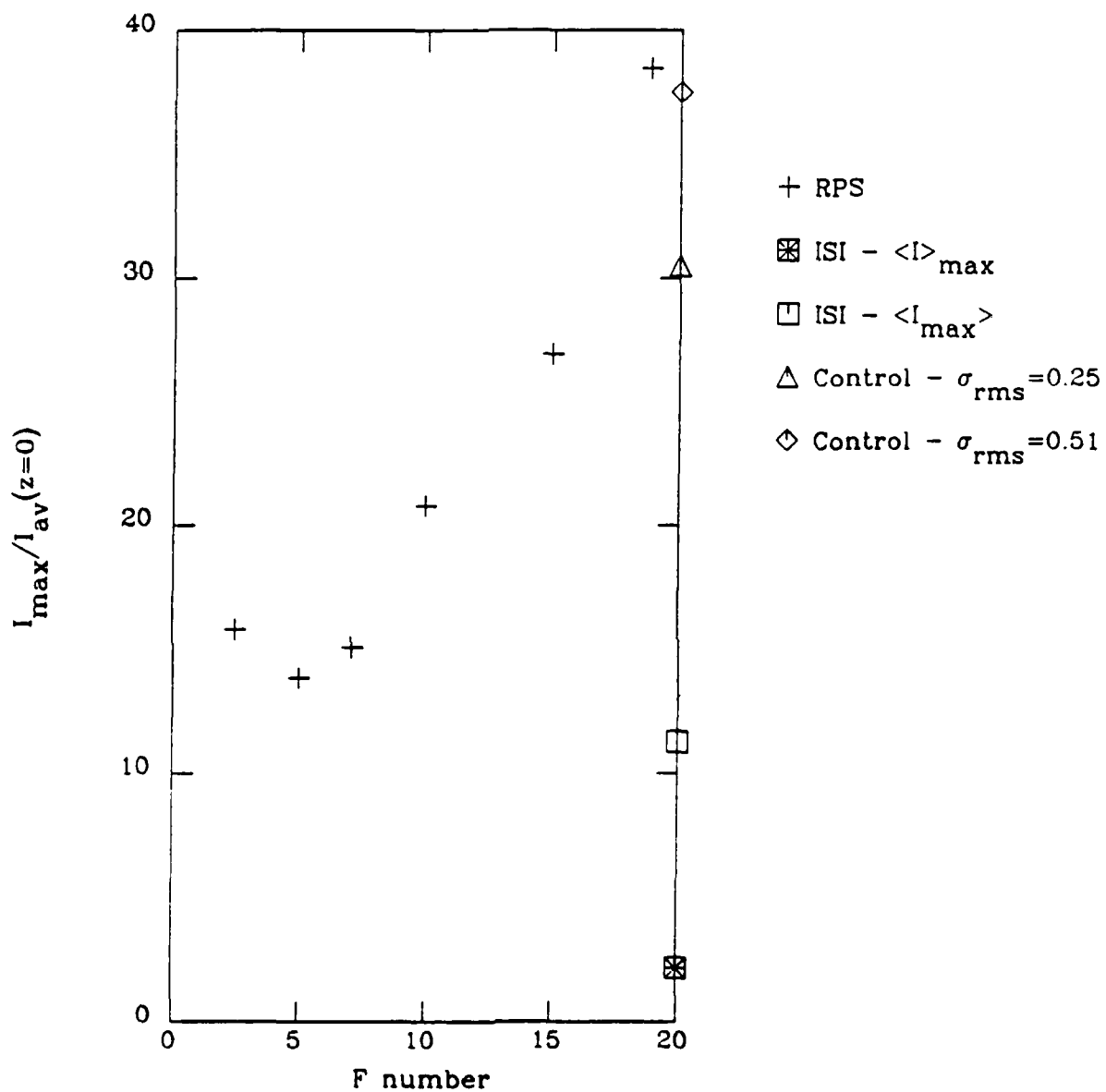
Figure 15 — Comparison of maximum intensity achieved inside plasma as a function of incident lens f number, for a variety of input intensity profiles.
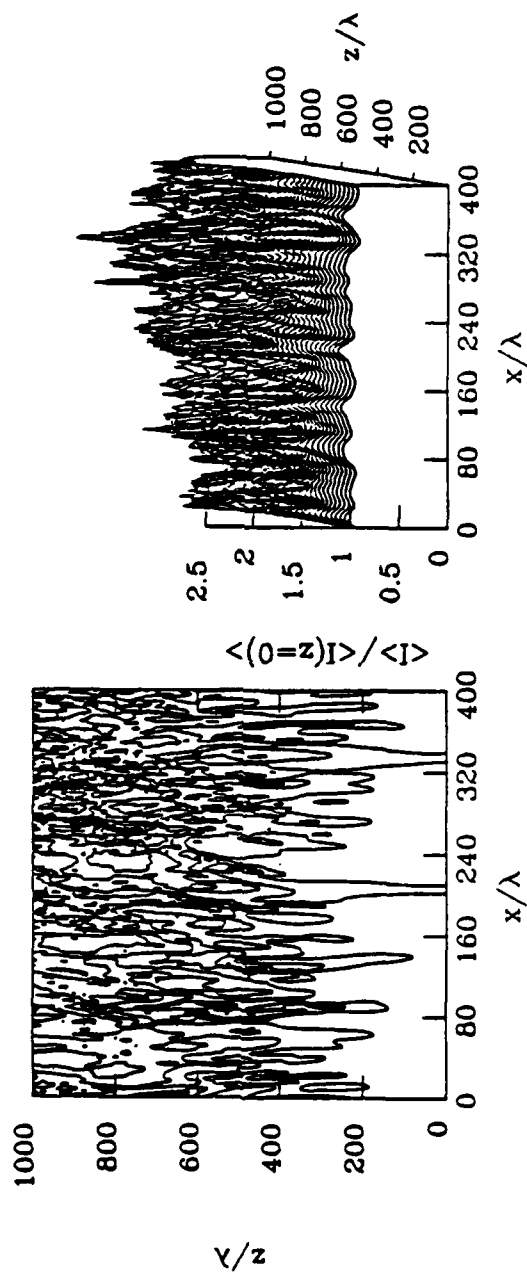
Figure 16 — Time averaged ISI laser intensity distribution incident on a slab of $.5n_{crit}$ CH plasma at 50keV. Average is taken over 350 coherence times.
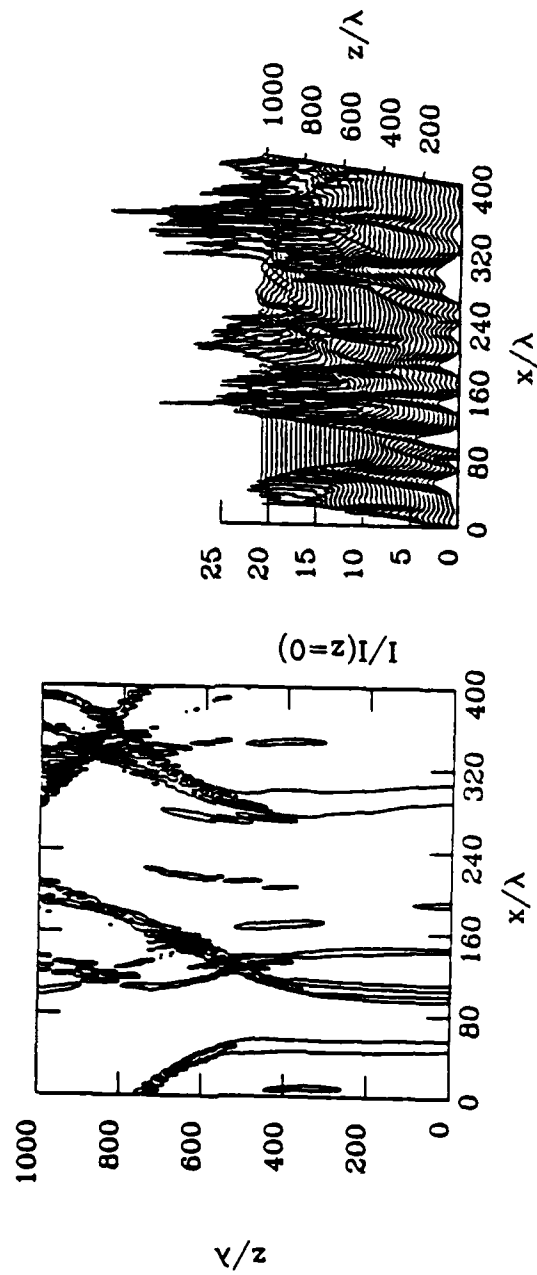
Figure 17 — Snapshot of the laser intensity at 350 t, for the same conditions as in Fig. 16.
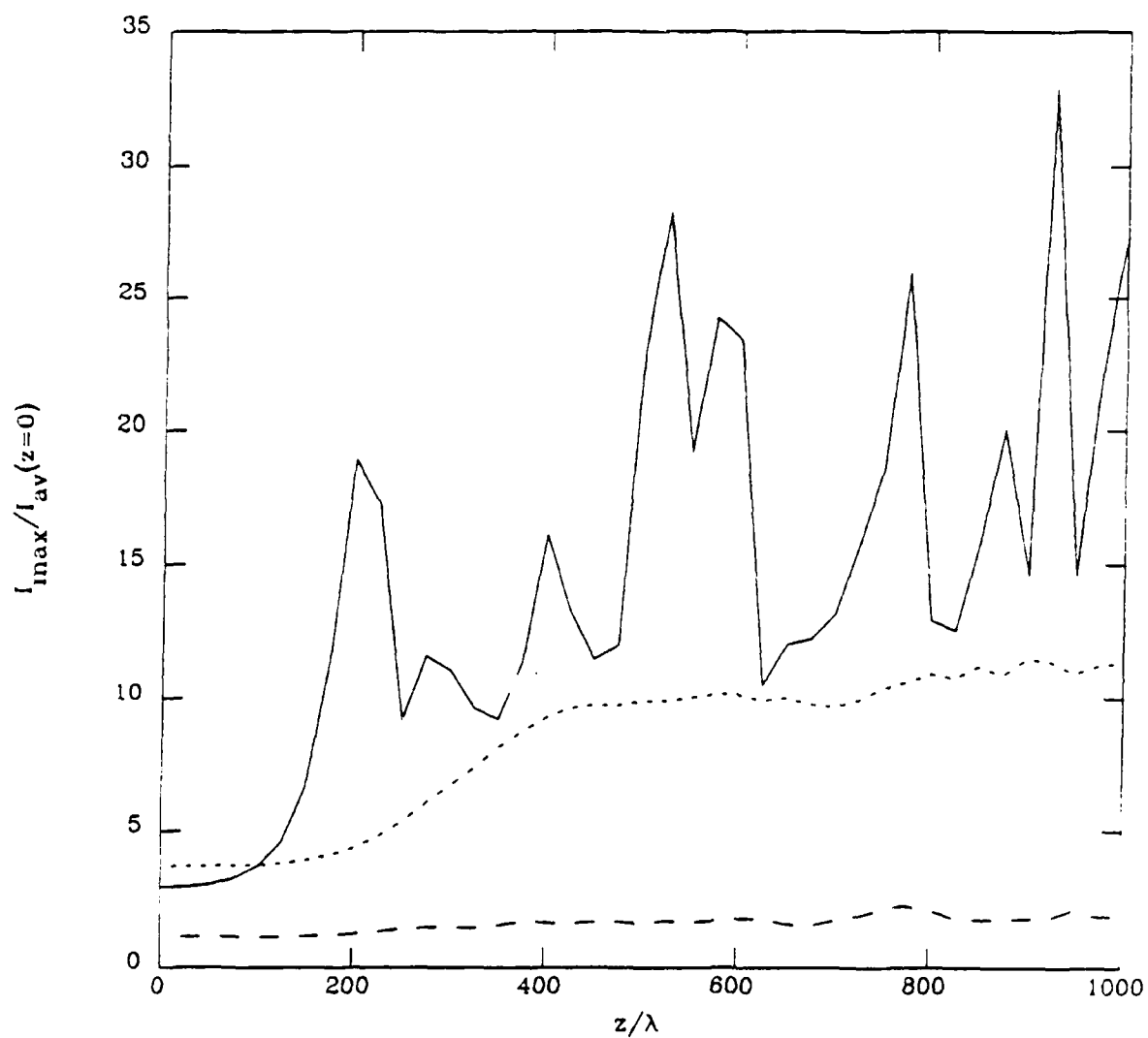
47

Figure 18 — Comparison of peak values of ISI and standard laser irradiation vs propagation distance in plasma. The solid line is the "typical" laser (3:1 peak-to-average incident intensity variations). the dotted line is the time averaged ISI intensity peaks ($\langle I_{max} \rangle$), and the dashed line is the maximum of the time averaged ISI distribution ($\langle I \rangle_{max}$).
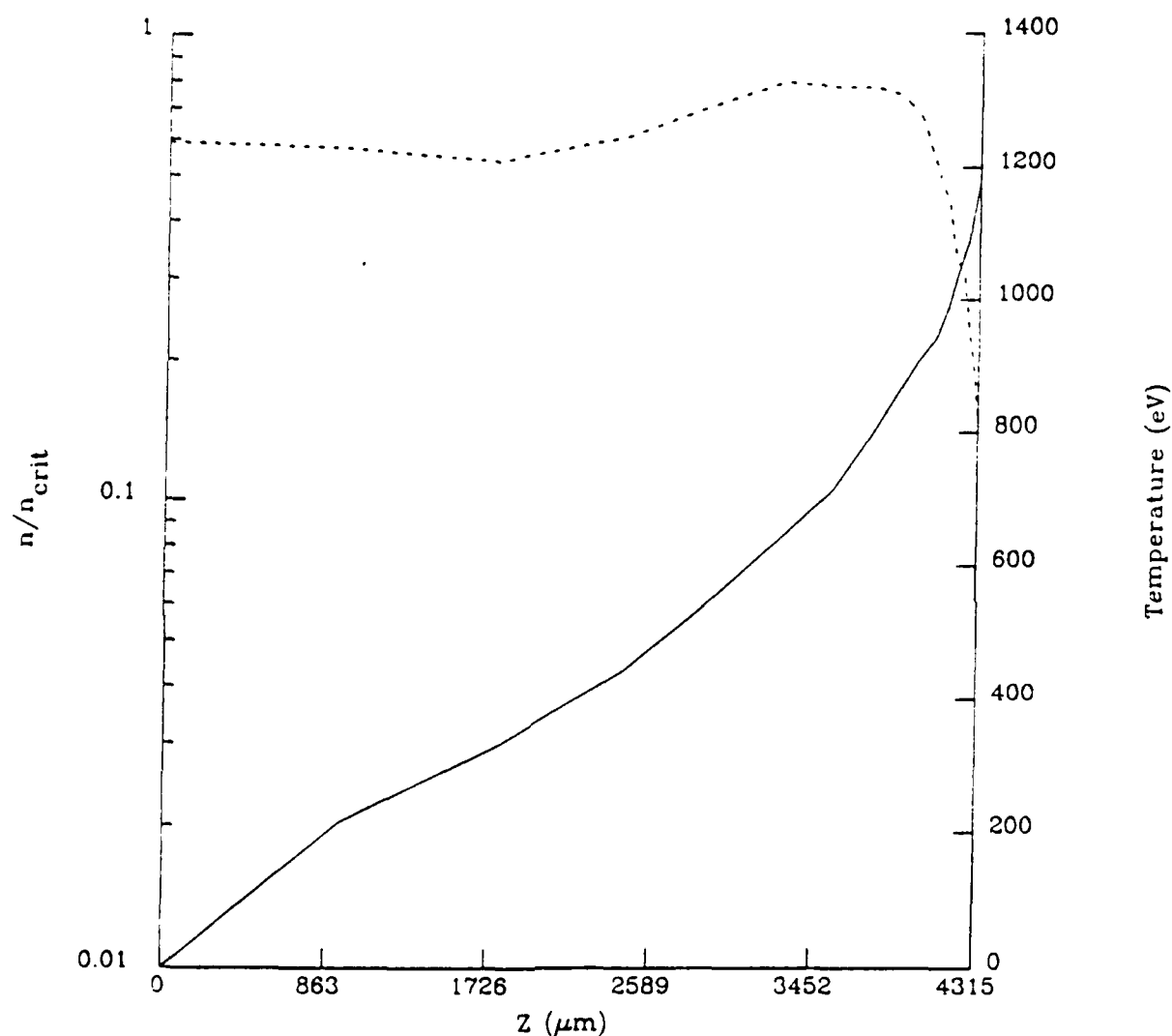
Figure 19 — Plasma electron density (solid line) and temperature (dotted line) profiles, taken from a simulation of a DT pellet irradiated by a KrF laser at 3×10^{14} W/cm^2. These are the conditions for the results pictured in figs. 20 and 21.
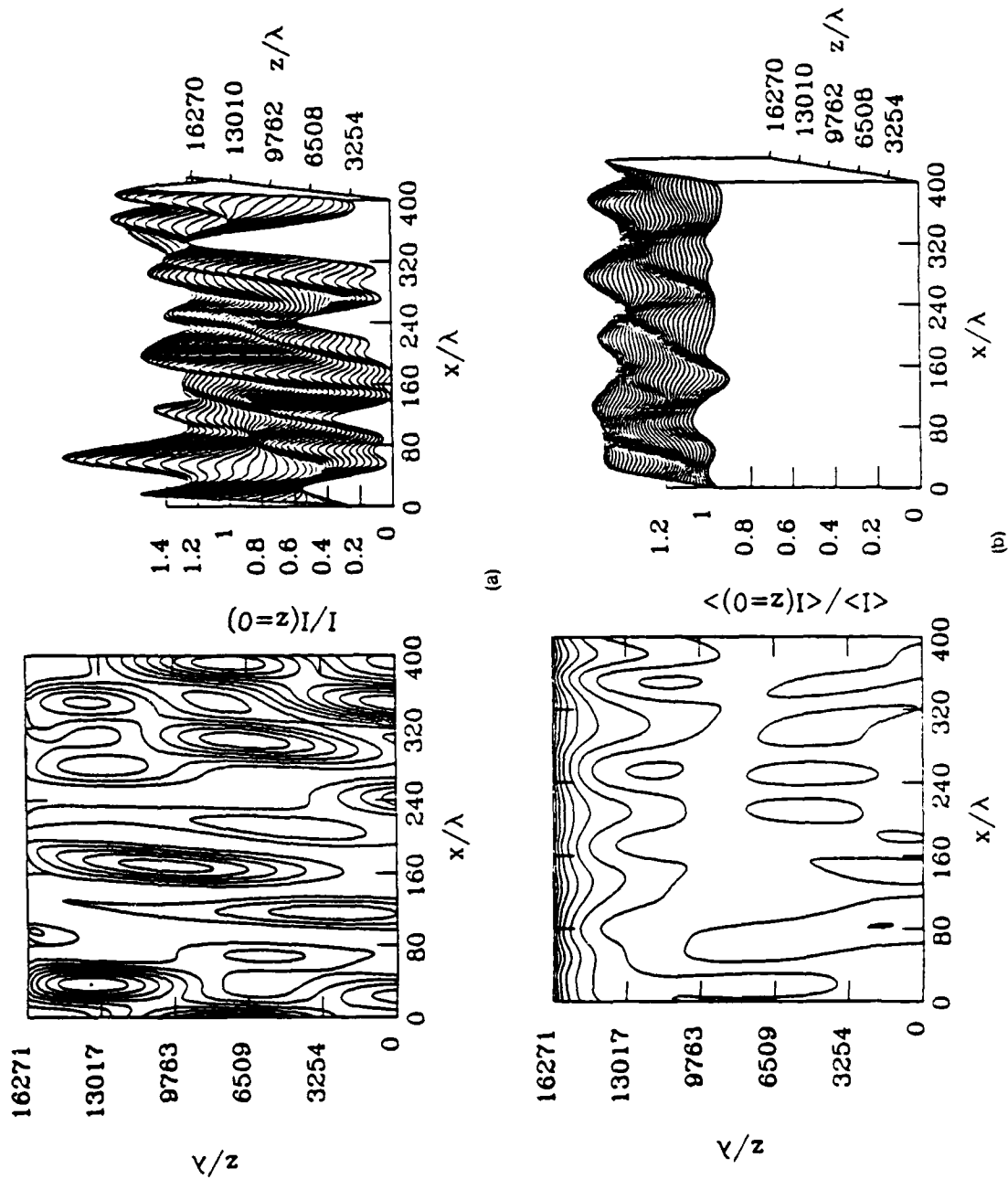
Figure 20 — Intensity distributions in the plasma (Fig. 19) irradiated with ISI laser (a) The instantaneous intensity after 500 coherence times shows no evidence of filamentation. (b) The time averaged intensity (over 500 t_c) shows very good smoothing by the ISI mechanism.
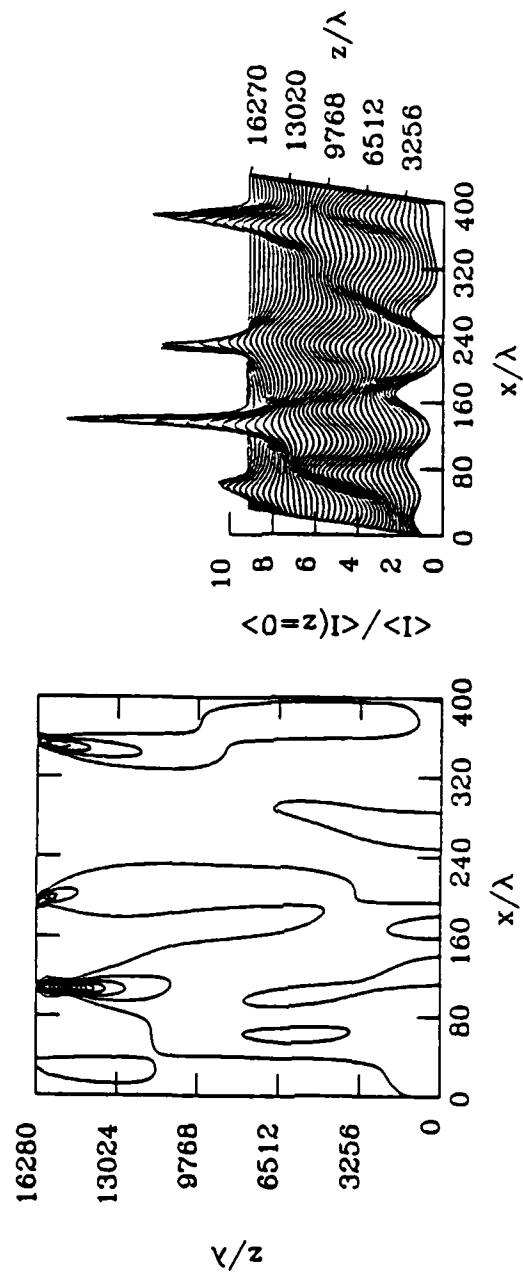
50

Figure 21 — The intensity distribution under the same conditions as Fig. 20, but with a typical laser profile incident (2.25:1 peak-to-average, $\sigma_{rms} = 0.5$ at $z = 0$).

51

INFORMATION NEEDED TO REPRODUCE F(r) IS TRANSPORTED THROUGH THE ABERRATED LASER BY A MULTITUDE OF SMALL COHERENCE ZONES
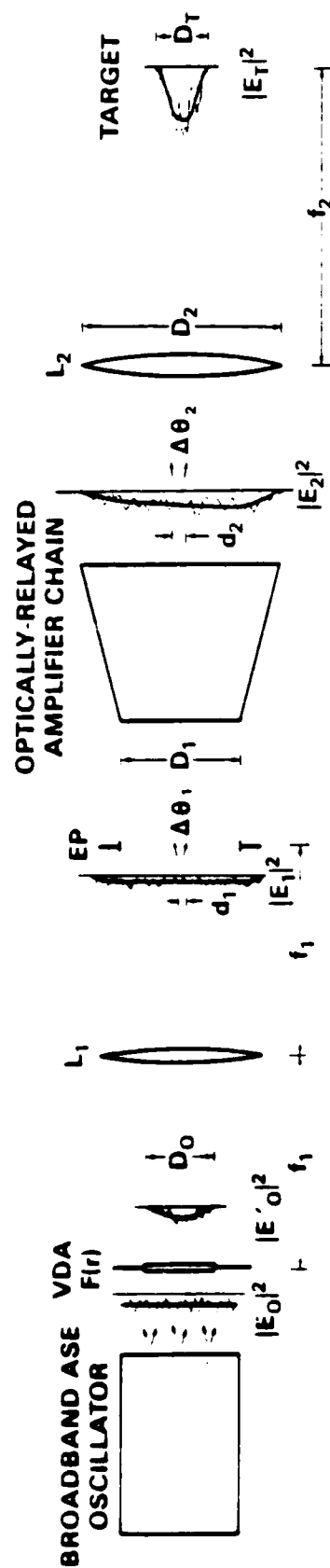

Figure 22   Schematic diagram of a spatially incoherent broadband laser system for smooth, controllable illumination of fusion targets   The fine line profiles show typical instantaneous intensities $|E|^2$, while the heavy lines show the time averaged intensities $|E|^2$

"Theory of Induced Spatial Incoherence"

DISTRIBUTION LIST

Dr. Y. Kato
Dr. K. Imasaki
Institue Laser Engineering,
Osaka University
Osaka 565, Japan

Dr. John E. Murray
Dr. John Lindl
Dr. Eric Storm
Lawrence Livermore National Laboratory
P.O. Box 5508
Livermore, CA 99550

Dr. J.P. Vandevender
Sandia National Laboratories
Albuquerque, NM 87185

S. Kahalas
R. Schriever
U. S. Dept. of Energy
Office of Inertial Fusion
Washington, DC 20545

Prof. M. Rosenbluth
Institute for Fusion Studies
University of Texas
Auston, TX 78712

Dr. John McLeod
Dr. Larry Blair
MS 548
Los Alamos National Laboratory
P.O. Box 1663
Los Alamos, NM 87545

Dr. R. Sigel
Abteilung Laser-Plasmen
Max-Planck-Institut für Quantenoptic
Postfach 1513
Boltzmanstrasse 2
D-8046
Garching bei München DB

53

Dr. Roger Haas
Applied Physics Dept.
University of California
Davis, CA 95616

Prof. Edourd Fabre
Prof. Guy Laval
Ecole Polytechnique
F-91128 Palaiseau
France

Dr. Robert Dautray
Centre D'etudes de limeil
Boite Postale No. 27
94190 Villeneuve, St. Georges
France

Dr. M. Key
Dr. P. O'Neill
Laser Division
Rutherford Appleton Laboratory
Chilton, Didcot, Oxon, OX11 0QX, United Kingdom

Dr. G. L. Kulcinski
Fusion Technology Institute
University of Wisconsin
Madison, Wisconsin 53706

Dr. S. Skupsky
Dr R.S. Craxton
Dr. R.L. McCrory
Laboratory for Laser Energetics
University of Rochester
Rochester, NY 14627

Dr. V. Happer
Physics Dept.
Jadwin Hall
Princeton University
P.O. Box 708
Princeton, NJ 08540

Dr. D. Pevitt
Dr. E Frieman
Science Applications Intl. Corp.
P.O. Box 2351
La Jolla, CA 92038

Dr. Roger D. Jones
MS-531
Los Alamos National Laboratory
Los Alamos, NM 87545

C. R. Menyuk
University of Maryland
College Park, MD

Alex Friedman
L-477
Los Alamos National Laboratory
Los Alamos, NM 87545

L. Vahala
Physics Dept.
William & Mary College
Williamburgs, VA 23185

J. Mark
LLNL
L-477
Livermore, CA 94550

R. Marchand
Dept. of Electro. Eng.
University of Alberta
Edmonton, Alberta
Canada

J. P. Matte
Monsier Tudo Wyatt Johnston
INRS-Energie
C.P. 1020, Varennes, QC, JOL 2P0

W.C. Mead
LANL
MS-E531
Los Alamos, NM 87545

Dr. R. Davidson
Plasma Fusion Center
Mass. Inst. of Tech.
NW16-202
167 Albany St.
Cambridge, Mass. 02139

Code 1220   1cp.

Code 2628   22 cps.

Director of Research
U.S. Naval Academy
Annapolis, MD 21402   2 cps.

R.H. Lehmberg

Code 4730   30 cps.

END
10-81
DTIC